DELFT UNIVERSITY OF TECHNOLOGY

BACHELOR OF SCIENCE THESIS
BSC APPLIED PHYSICS
FACULTY OF APPLIED SCIENCES

Flux-behaviour and Resistances of Electroactive Material in a Semi-Solid Flow Battery Cell

Author
Rinus Smit

Supervisor
Dr. Martin Rohde
Second Examiner
Dr. Erik Kelder

September 27, 2020

Abstract

Renewable energy sources such as solar and wind are being deployed in larger amounts than ever before as alternatives to classic energy sources. A familiar problem with these type of energy generating systems is the lack of the ability to rapidly react to demand fluctuations.
Conventional rechargeable batteries offer a simple and efficient way to store electricity, but the focus of the development of these batteries has largely been on smaller systems than can facilitate portable power or intermittent backup. For grid storage, metrics relating to volume and size are far less critical than in transportation and portable power systems. Flow batteries can provide a better performance for reduced costs in large-scale energy storage of electrical energy.
Redox Flow Batteries (RFBs) are a type of flow batteries that can be implemented in facilities where large-scale electrical energy storage is desirable. However, the main problem with Redox Flow Batteries is that they are based on electroactive ionic species dissolved in aqueous solvents, which implies a low concentration of active material.
A solution to this problem comes in the form of Semi-Solid Flow Batteries (SSFBs), a new approach to flow batteries that uses suspensions of solid energy-dense active material and Carbon Black particles in a liquid electrolyte. The advantages in design of flow batteries are kept and the energy storage density can be up to ten times that of RFBs. The disadvantage of using these suspensions is the complex electronic behaviour and increase in viscosity of the suspensions by using solid electroactive particles and solid Carbon Black particles instead of solutions with dissolved ionic species.

In order to allow for further development of SSFBs, a better understanding of SSFBs suspensions is needed to increase the performance and efficiency of the system. Earlier done rheological and electrical research on $LiCoO_2$ and $Li_4Ti_5O_{12}$ suspensions at varying shear rates is used to study how the ionic flux of the active species behaves and how electronic and ionic resistances are built up.
The ionic flux facilitated by convection through the cell is studied and compared to the flux of ions towards the membrane of a SSFB flow cell due to migration. The ionic flux due to convection is found by calculating velocity profiles from viscosity data from earlier done research on SSFB suspensions. These velocity profiles are evaluated and used to calculate the convection term in the Nernst-Planck equation.
The ionic flux due to migration is found by determining how the resistances in a SSFB system are built up and what the contribution of every component in the suspension to these resistances is. The total electric resistance in the system is divided into three parts: electronic resistance, internal ionic resistance and external resistance.
The electronic resistance is calculated from electronic conductivity data originating from the same earlier done research on flow cells in discharge with an imposed potential difference. The external ionic resistance of the suspensions is calculated from the ionic conductivity of Li-ions in the corresponding electrolytes. From a calculated assumption for the current through the system and with Ohm's law, the potential drop due to each of these resistances is determined. As the potential difference over the entire cell was imposed beforehand, the electronic and external ionic potential drop are subtracted from the total potential difference. This leaves the potential drop from the internal ionic resistance, the latter of which can be computed by again using Ohm's law.
The ionic flux due to migration in the Nernst-Planck equation is calculated from total ionic resistance. With this, the resistances in the system as well as the ionic convection flux and ionic migration flux for multiple suspensions are known. A final calculation is determining the Rohde ratio, which determines the fraction of ionic axial flux (convection) that leaks away towards the membrane due to migration. It also shows if the assumption that the concentration Li^+-ions throughout the cell remains constant is valid.

It is found that the internal ionic resistance has the largest contribution to the overall resistance in the system. This can be attributed to the high resistance an ion experiences as it is transported out of the electroactive particle. The assumption about the concentration proved to be incorrect. The Rohde ratio showed that a substantial amount of ions leaks away due to migration, meaning the concentration in the flow cell varies. It is also shown that ionic flux due to migration increases when more electroactive material is present.
Keeping a balance between optimizing electronic conductivity and suspensions viscosity must have priority in order to develop improved SSFB systems. It is recommended to study the complex interactions between electroactive material and Carbon Black particles to find what suspension contents are optimal for battery performance.

Contents

1 Introduction

1.1 Need for energy storage

Currently, worldwide efforts are devoted to support an efficient use of renewable energy sources and sustainable electrical transportation. Renewable energy sources such as solar and wind are being deployed in larger amounts than ever before as alternatives to classic energy sources. Flow batteries provide a solution in storing energy from renewable sources for discharge during periods of peak demand. They can also be deployed at power stations as support by storing excess electrical power during low demand periods, which can in turn be used as demand rises. Another useful application of flow batteries is as stand-alone power systems for isolated grids and remote villages. [1]
Conventional rechargeable batteries offer a simple and efficient way to store electricity, but the focus of development has largely been on smaller systems that can facilitate portable power or intermittent backup power. Batteries for large-scale grid storage require an ability to respond rapidly to changes in load or input, endurance for a large number of charge and discharge cycles, high round-trip efficiency and feasible costs. Flow batteries promise to meet many of these requirements and therefore form a valuable solution to support renewable energy sources and other electrical energy facilities. [2]

1.2 Conventional static batteries

Batteries are available with different battery voltages, capacities, costs, energy densities, geometries, power densities and so on, all being developed depending on the application. [4] Because of their high energy density and long life-times [3], rechargeable lithium ion (Li^+) batteries have found their way in a great variety of systems such as electric vehicles [5], portable electronics [6], space and aircraft power systems [7] and stationary power storage [8].
A Li-ion battery consists of current collectors to transport electrons from the current collectors to the battery terminals, a positive current collector (cathode), a negative current collector (anode), ionic-transport-providing electrolyte that maintains charge neutrality during charge and discharge and a separator that prevents shorting of the electrodes. [4] The separator is a porous, insulated membrane through which lithium ions can be transported. [9] Figure 1.1 shows a schematic overview of a conventional static rechargeable battery.

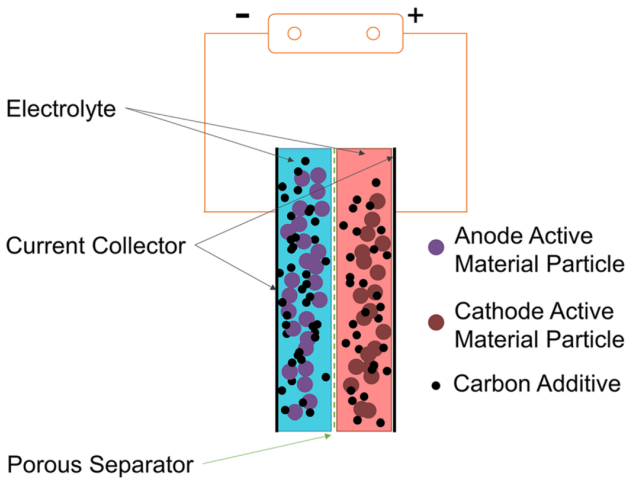

Figure 1.1: Schematic overview of a static rechargeable (Li-ion) battery. [4]

Lithium-ion battery materials require both ionic and electronic conductivity for storing and providing electrical energy via redox electrochemical reactions during charge and discharge. [11] During charging, the active cathode material is oxidized as to release electrons and lithium ions. During discharging, the cathode material is reduced based on the reverse reaction. [10] The overall process can be summarized by [10]:

$$xLi^+ + A_zB_y \xrightarrow{\text{charge}} Li_xA_zB_y. \tag{1.1}$$

The process runs the opposite direction in discharge. The electrolyte carries positively charged lithium ions from the cathode to the anode and vise versa through the membrane. Because the active material often lacks electronic conductivity, carbon additives are mixed with the active particles to facilitate electronic transport to the electrode. [11] Two examples of materials that comprise the active material in the cathode are $LiCoO_2$ (LCO) and $Li_4Ti_5O_{12}$ (LTO). [13]
As mentioned, rechargeable batteries have largely been developed for transportation or portable applications. For grid storage however, metrics relating to volume and size of batteries are far less critical than in transportation systems and systems for portable power. Redox flow batteries can provide a better performance for reduced costs in large-scale storage of electrical energy. [2]

1.3 Storage on large scale: Redox Flow Batteries

In Redox Flow Batteries (RFBs), fluid materials are stored in external tanks and are pumped through an electrochemical reactor (electrochemical flow cell) in which ion-exchange and electron-extraction takes place. A redox flow battery system contains aqueous electrolyte with one or multiple dissolved electroactive materials from which power can be extracted from the electrochemical reaction. A schematic representation of a redox flow battery can be seen in figure 1.2.

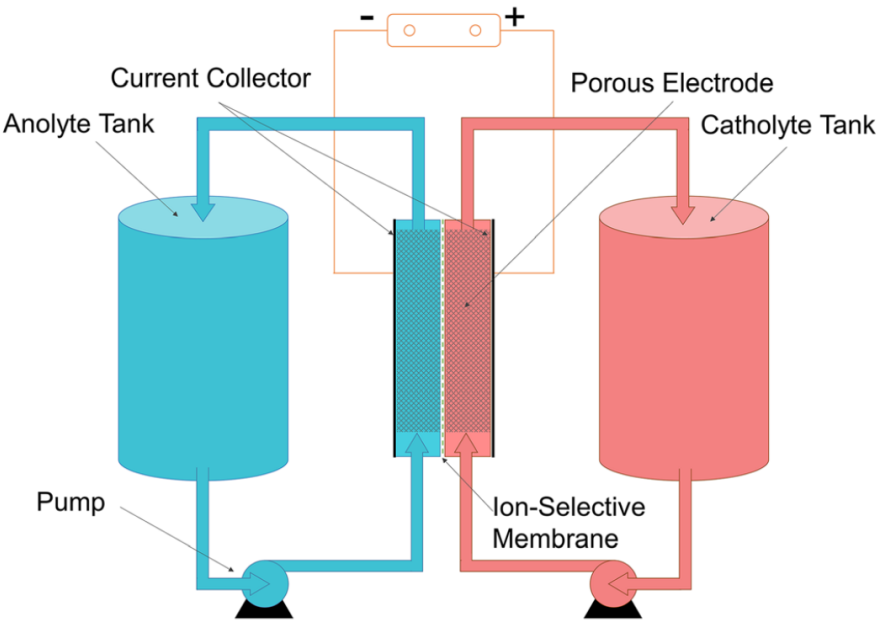

Figure 1.2: Overview of a Redox Flow Battery system. [4]

The electrochemical reaction is a reversible process, meaning that the stored electrochemical energy can be converted into electricity and can be stored again. This is what makes an RFB rechargeable.
Inside the electrochemical cell, reduction-oxidation (*re-dox*) reactions take place between the dissolved electroactive particles of the catholyte and anolyte. When discharging, an anolyte solution flows through a porous medium in the cell and reacts to generate electrons, which flow through the external circuit. The charge-carrying species are transported through a seperator (which typically is an ion-exchange membrane) in the flow cell to the catholyte. The pumps of an RFB ensure that the active materials are replaced constantly, maintaining electric current in the system. [2]
An RFB has a unique ability that allows for decoupling the stored energy and power. The size and volume of the tanks and the concentration of the electroactive species determine the energy of the system, while the size of the electrochemical flow cell, the surface area of particle exchange and the flow rate are responsible for the power the system can deliver. For stationary applications where large-scale batteries are desirable, this gives a significant freedom in the design of a RFB, making it a suitable candidate for the implementation of large-scale energy storage in existing systems such as wind and solar. [16]

The disadvantage, however, is that most RFB systems are based on electroactive ionic species dissolved in aqueous solvents, which implies that the concentration of active material is low and the potential window is limited. [2] This means that advantages in the freedom of the design of the flow cell are negatively balanced by the use of low-energy density active materials. [13]
A new approach for flow-cell batteries was proposed in 2010 by Chiang et al. [14], which involves using lithium-ion battery materials. Solid electroactive particles with carbon black are suspended in a liquid Li^+-containing electrolyte. This semi-solid flow cell has been demonstrated to have an energy density ten times higher than those of classical RFBs. [16]

1.4 Storage on large scale: Semi-Solid Flow Batteries

The semi-solid flow battery (SSFB) can be thought of as a hybrid between a conventional rechargeable Li-ion battery and a redox flow cell. The working principle of the SSFB is equivalent to that of the RFB, with the main difference being the types of catholyte and anolyte that are used for electrochemical power and storage. A visual representation of an SSFB can be found in figure 1.3, which is analogous to the RFB system shown in figure 1.2.

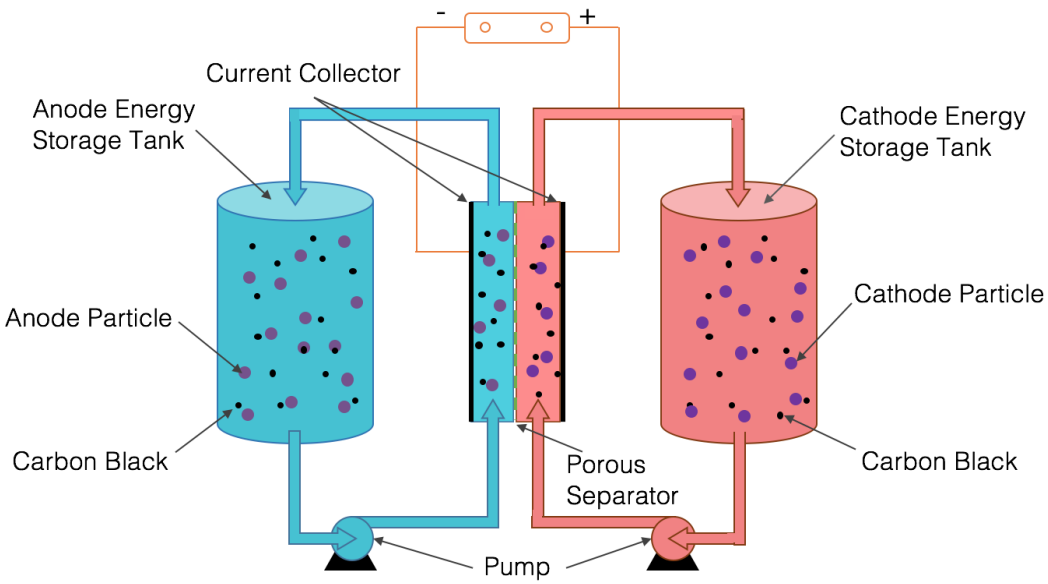

Figure 1.3: Overview of a Semi-Solid Flow Battery system. The denoted active particles represent the solid active materials. [4]

An SSFB uses suspensions of energy-dense active materials in a liquid electrolyte, while maintaining the advantages of a flow architecture type battery. Since the introduction of the semi-solid flow battery by Chiang et al. [14], the properties, behaviour and performance of these new type of battery systems are studied and are tempted to be understood [13] [15] [16] [17]. Due to the use of solid-storage active materials, an SSFB can produce ten times the charge storage density of typical flow solutions. [16] [17] Compared to the volumetric capacity of aqueous redox solutions ($\approx 2M$), the suspensions have a volumetric capacity that is 5-20 times higher ($10M$ to $40M$). [13] The energy density of the catholyte or the anolyte is no longer constrained by solubility limitation, but rather by the allowed fraction of active material solids in the flowable suspension. The electronic transfer of active particles is achieved by the addition of carbon black powder, which brings the electrons from the current collectors to the active particles and vice versa via a percolated network.

Nonetheless, the SSFB system also has obstacles that need to be understood and dealt with before it can be implemented in above-mentioned applications. A major obstacle in the use of SSFB suspensions is, for example, the significant increase of the viscosity as the different suspension components are put together. This in turn one of the factor that decreases the efficiency of the system as energy is needed for pumping the suspension. [17] [18]
The performance of a flow battery system depends on the types of solutions or suspensions used, the

flow rate, the concentration of electroactive particles, the concentration of carbon additives, the ion-exchange membrane and its surface and the factors that contribute to energy losses. The viscosity of the suspension for example influence the resistance for the suspension to flow and the ease of electrons to be transported depends on the carbon additives. [2] [16] [19]

To get a deeper understanding and to optimize the performance of semi-solid flow batteries, it is helpful to study the behaviour of the active materials and their relation to battery performance. Previous articles like Qi et al. (2017) (which is a review paper on flow battery systems with solid electroactive materials) discuss more research must be done on fluid viscosity and electronic conductivity to reduce overall resistance and increase battery performance. Mainly, research has been done on the viscosity and electronic conductivity of certain types of suspensions (like Duduta et. al (2011) and Youssry et. al (2013), without looking at what are the contributions of the resistances in the system and in what ways they can be improved. The main focus of this thesis will be to look into these different aspects of the resistances and how they influence the behaviour of electronic and electroactive particles in Semi-Solid Flow batteries. With that, the ionic flux of the active species is looked into to see how it is influenced by the different contributions in the Nernst-Planck equation.

1.5 Problem description

Research on SSFB systems that has been conducted has been centered around studying the behaviour of different types of suspensions, different types of carbon additives and optimizing the performance of the battery overall. In order to develop a better understanding of SSFB systems, data from earlier performed research by Youssry et al. [19], Duduta et al. [13] and Madec et al. [16] will be used to study the way active material (Li^+) and electrons are conducted in the system and how the flux of electroactive species and their resistance to movement is influenced by varying suspension concentrations, flow rates and type of active species used. This will be done by evaluating contributions to the Nernst-Planck equation, a mass transport equation used to describe the motion of charged chemical species in a fluid medium.

1.6 Report description

The report is structured as follows. In the chapter following, the working principles of the SSFB, the behaviour of non-Newtonian fluids and the Nernst-Planck equation are explained. Chapter 3 discusses the methods used to determine the different contributions to the flux of active particles from research data. The results from the performed research will be displayed and reviewed after. In chapter 5, the Discussion, both the research results and the SSFB system as a whole are critically examined and looked upon more deeply. This chapter is followed closely by recommendations. The last chapter describes the conclusions that can be drawn from the results.
At the end of the report, the appendices contain conductivity profile results in a flow cell, an additional model used to determine ionic flux near a ionic membrane and additional images and data from SSFB systems.

2.1 Semi-Solid Flow cell principles

2.1.1 SSFB design

The basic components of the semi-solid flow battery are similar to the components of a redox-flow battery. The center of the SSFB is a flow cell at which the electrochemical reactions take place during charging and discharging. To get a complete view of the system, the flow cell is taken as basis from which the rest of the system is described. Figure 1.3 can be used as a reference for the explanation that follows.

The flow cell contains two compartments through which suspensions can flow, divided by a porous ion-exchange membrane. As mentioned before, the membrane prevents shorting of electrons to the two different current collectors on the outsides of both flow chambers. One of the flow chambers contains catholyte, while the other contains anolyte. The current collectors direct the captured electrons via the external circuit to the oppositely charged current collector. The direction of the electrons depends on the state the battery is in: either charging (plus to minus) or discharging (minus to plus). The current collectors are typically made of copper and aluminum. [13]
Flow cell batteries are a way of increasing power and amount of energy that can be stored in comparison to a conventional battery. The amount of energy is increased with the use of external tanks that are connected to the flow cell. The tanks contain the electroactive material, which is pushed through the system using pumps between the flow cell and the tanks. Once the suspension material exits the flow cell, it is redirected back towards the tanks. Of importance to note is that the catholyte and anolyte are stored in separate tanks - the electrochemical reactions that store of produce electrical energy would otherwise occur in the tanks, where it cannot be extracted the same way as in the flow cell.
The advantage of a flow battery is the ability of the tanks to decouple from the system. The tanks can be recharged externally, while other *charged* tanks can take over. This allows for the system to store electrochemical energy which can be transported elsewhere or used in a time of need.

2.1.2 Chemical reactions

Electrochemical energy in flow-batteries is stored and used via redox-ractions. In principle, a redox-reaction (reduction-oxidation) is a type of chemical reaction that involves transfer of electrons between species. With (increase of) oxidation electrons are lost, meaning an increase in the oxidation state of an atom or an ion. With reduction electrons are gained, meaning a decrease in the oxidation state of an atom or an ion. The following is an example [4] of a redox reaction in a conventional static battery with $LiCoO_2$ as cathode and LiC_6 as anode

$$CoO_2 + Li_+ + e^- \longrightarrow LiCoO_2 \tag{2.1}$$

$$LiC_6 \longrightarrow C_6 + Li^+ + e^- \tag{2.2}$$

which give the total redox-reaction

$$LiC_6 + CoO_2 \longrightarrow C_6 + LiCoO_2. \tag{2.3}$$

During discharge in the flow batteries, the anolyte releases Li^+-ions and electrons. The Li^+-ions are transferred through the membrane to the catholyte, while the electrons are extracted from the anolyte by the current collector. The electrons run through an external circuit towards the oppositely charged current collector, where they will be able to complete the redox reaction. During charging, the exact opposite happens in order to store energy. The flow of electrons is what gives rise to current.

2.1.3 Electrolyte and redox-active compounds

In static batteries and flow batteries, active species are dispersed in electrolyte and are often surrounded by carbon additives. Li^+-ion batteries stand out among rechargeable battery materials with regards to energy density and duration of cycle re-usability. Well-known Li^+-ion battery materials for example are lithium cobalt oxide ($LiCoO_2$, or LCO) and lithium titanate oxide ($Li_4Ti_5O_{12}$ or LTO) which act as the

active materials in a battery (flow) cell. During the charging process, Li^+-ions are transferred from the cathode to the anode (and are transferred in opposite direction during discharge). [4]

The transfer of ions in a battery is facilitated by an electrolyte with soluble salts, acids, bases or polymers. The electrolyte acts as a catalyst to make a battery conductive by stimulating the movement of ions through the electrolyte. An electrolyte must be stable in order for this process to work in a desired way, which means that is has non-reactivity with the active species [13], that it is resistant to fluctuations in temperature and that is has a substantial electrochemical window. [2] The electrochemical window is the voltage range in which a substance is neither oxidized nor reduced. This window is of importance for the type of electrolyte used in batteries and for the battery efficiency, because if out of this voltage range, electrolysis of the electrolyte occurs. This consumes energy that is intended for the desired other electrochemical reactions in the battery. [13] [16]

Another feature of the electrolyte with dissolved salt is to keep the flow cell electrically neutral by providing Li^+-transfer. Often, organic solvents replace water as electrolyte, for they provide larger stability windows to increase net cell voltage and subsequently the battery performance. This has been the drive behind the use of organic solvents, despite the cost and flammability of organic solvents. [4]

As mentioned, the energy densities of SSFB suspensions are significantly higher than the energy density of solutions used in redox flow batteries. The electroactive particles used for an SSFB are solid, which means solubility limitations are not longer relevant, though the trade-off between electrolyte viscosity and particle loading is still a major consideration. [4]
As the concentration of the active species increases, the viscosity of the electrolyte increases and the energy lost to pumping increases. [4] An example of an electrolyte with high viscosity can be found in Appendix C, figure C.1 which is a photo of a semi-solid suspension containing $LiCoO_2$ powder as the active material and Ketjen black as the conductive material, dispersed in alkyl carbonate electrolyte [13]. The addition of carbon black particles is essential for electronic transfer in the flow cell, but as will the explained in the following section, it plays a major role in the viscosity increase of the suspension.

2.1.4 Carbon Black particles and network formation

Carbon Black particles play a key role in the electrical conductivity in a battery (flow) cell and are widely used due to their low cost, chemical stability, availability of a range of particle shapes and sizes and compatibility with processing conditions. Different terms are used to describe CB particles and there formations: particle, aggregate and agglomerate. Initially, CB is formed as spherical particles which covalently bond to form structural units in a CB suspension. These units are called aggregates. Under the influence of Van der Waals forces, the aggregates can bind together in agglomerates which typically have a size of 10-100 μm. The magnitude of the binding force depends on the chemical properties of the CB particles, the inter-particle interaction and interaction with the suspension media, which all may change the agglomerate shape and size. [19]
Above a certain critical concentration of CB particles, a three-dimensional continuous network of particles is formed. Above this concentration, the suspension is highly viscous and has considerable conductivity. The critical concentration is called the percolation threshold. [19] The formation of these networks is highly dependent on the shear rate of the suspension as it is pumped through the flow cell. The shear rate $\dot{\gamma}$ is the rate at which fluid layers move past each other. Below, a exmaple can be found in figure 2.1 that illustrates the electrical and rheological behaviour of the suspension in a flow cell measured at different shear rates, with a focus on the size and shape of the agglomerations that are formed by CB.

What becomes evident is that different sizes and shapes of agglomerations are formed at different shear rates:

1. Long agglomerations (low shear rates) - high conductivity;
2. Intermediate agglomerations (intermediate shear rate) - low conductivity;
3. Short agglomerations (high shear rates) - increased conductivity.

At rest and low shear rates, the CB network is well constructed so that the density of chains is high enough to transfer electrical current. Shearing (with intermediate shear rates) the suspension makes the conductivity drop, which implies breaking of the network and formation of smaller agglomerations. At

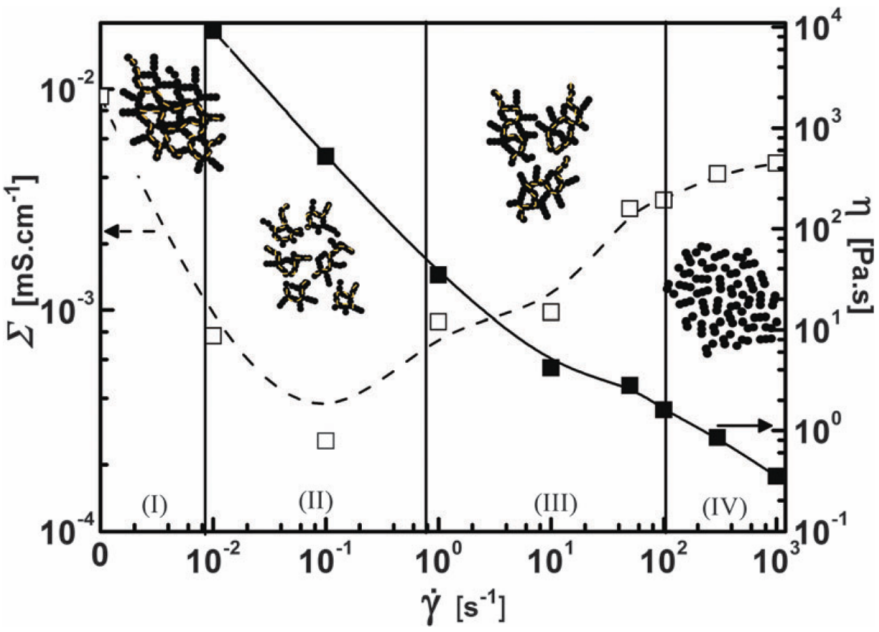

Figure 2.1: The conductivity (dashed line) and viscosity (bold line) of a $\phi_{KB} = 0.021$ (volume fraction) suspension in a redox flow cell at different shear rates. Σ denotes the conductivity, η is the viscosity and $\dot{\gamma}$ is the shear rate. Plot is used from Youssry et al. (2013). Added are schematic drawings of the several states of CB within the CB suspension: (I) a 3D network of agglomerates; (II) breakup of the network into agglomerates; (III) formation of hydrocluster agglomerates; (IV) erosion into small agglomerates or even single aggregates. Before recording the rheological data, the suspension sample was left to rest for 1 h. This was done in order to eliminate effects of shear history, which could have a profound impact on the experiments. [19]

high shear rates, much smaller agglomerations or even single aggregates are formed which decreases the viscosity but increases the density of effective chains. This results in an increase in conductivity, for the suspension flow at such a velocity, that small agglomerations are constantly loosely connected. This creates an effective chain that is not connected together strongly, but is structured is such a way that the gaps between the agglomerations are small enough for electrons to tunnel through. [19]

Different types of CB are available for electrochemical applications. Ketjen Black (KB) and Super C45 (C45) are two examples of CB used in (flow) batteries. These particles differ in size and shape, as can be seen in the TEM microscopic images in figure C.2 in Appendix C. The types of CB differ in size, density and surface area, which means differences in rheological and electrical behaviour in suspensions. In choosing a certain type of suspension for a flow battery, the choice of type of carbon additive must therefore be taken into account when composing a suspension. There is for example another additive: Carbon-Nano Fibers (CNFs), which electronically wires the conductive pathways and even reduce viscosity of the suspension electrode [16].
In Youssry et al. (2013), lower rheological and electrical percolation thresholds are found for KB compared to C45. This is why the choice of KB is preferred in flow batteries, confirmed in [13] and [16] and in the Results section. Additionally, the conductivity profiles of two types of suspensions used in Youssry et al. (2013) are presented figure A.1 and A.2 in Appendix A as a confirmation of the lower electrical performance of C45 compared to KB.

2.2 Rheology of suspensions

2.2.1 Non-Newtonian fluids

The bold line in figure 2.1 shows the viscosity of a suspension used in a redox flow cell with a volume fraction of $\phi_{KB} = 0.021$ measured at different shear rates. The viscosity of this material is strongly

dependent on the shear rate of the flow. A fluid that has viscosity changing under an external force is called a non-Newtonian fluid. Simply put, a non-Newtonian fluid does not follow Newton's law of viscosity. Newton's law for viscosity is written as:

$$\tau = -\mu \frac{du_i}{dy_j} \tag{2.4}$$

in which τ [N m^{-2}] represents the shear stress, μ [Pa s] stands for the constant viscosity and $\frac{du}{dr}$ [s^{-1}] the velocity gradient. [12] The shear stress τ is an example of an tangential force, acting along the surface of a fluid layer. The surface of a fluid layer is defined to be in the direction of flow. Shear stress arises primarily from fluid viscosity. For non-Newtonian fluids, the viscosity μ is not constant and depends on the shear rate of the fluid layers. The expression for the viscosity (now denoted with η) is:

$$\eta(\dot{\gamma}) = K\dot{\gamma}^{n-1} \tag{2.5}$$

and because the shear rate $\dot{\gamma}$ is defined as the rate of change of the velocity at which one fluid layer passes over an adjacent fluid layer (or the modulus of the velocity gradient) equation 2.5 can be written as [12] [13]:

$$\eta(\dot{\gamma}) = K\left|\frac{du_i}{dy_j}\right|^{n-1}. \tag{2.6}$$

η is called the apparent viscosity in [Pa s] and uses a different symbol than is used for the constant viscosity to make a clear distinction between the two of them. K in [Pa s] is a constant that stands for the consistency and n is the flow index. The flow index is a constant that determines under which category a fluid can be placed. For n < 1, the fluid shows shear-thinning behaviour. For n $= 1$, the fluid behaves as a Newtonian fluid. For n > 1, the fluid shows shear-thickening behaviour. In case n $\neq 1$, equation 2.6 must be used to determine the fluids viscosity. Figure 2.2 shows the relation between the shear rate and velocity gradient for different types of fluids.

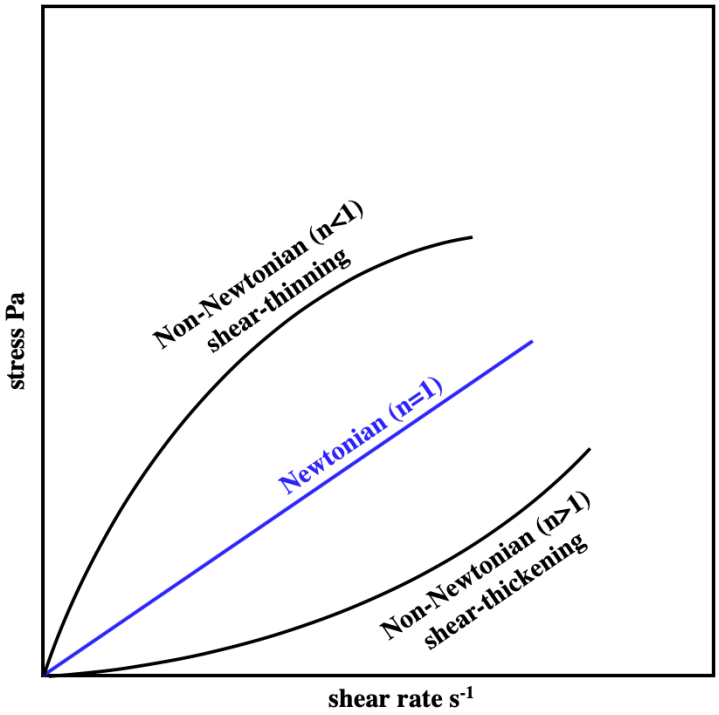

Figure 2.2: Relation between the shear rate and velocity gradient for different types of fluids.

Together with equation 2.4 and equation 2.6, the shear stress for non-Newtonian fluids can be determined by the following expression [12]:

$$\tau_{y,x} = -K\left|\frac{dv_x}{dy}\right|^{n-1}\frac{dv_x}{dy}. \tag{2.7}$$

Section 2.3.2 will discuss how this expression for τ is used to determine the velocity of a viscous non-Newtonian fluid in a flow cell.

2.2.2 Viscous electrolyte

The suspensions used in SSFB systems consist of different types of particles that contribute to viscous behaviour. The viscosity of the suspensions is highly sensitive for suspensions with either differing amounts of Ketjen Black, differing amounts of LCO or both. A suspensions that contains 0.3-0.6 vol$\%$ (volume fraction) KB produces strong shear-thinning behaviour indicative of network formation, whether the suspension contains Ketjen Black alone or LCO at 22.4 vol$\%$ or 40 vol$\%$. The viscosity is in fact several-fold higher for suspensions containing both solid particles (KB and LCO) than either suspension alone. This indicates complex interactions between the CB and electroactive particles. [13]

Scanning Electron Microscope (SEM) micrographs of LTO2KB suspensions with Carbon Nanofibers (CNF) can be found in Appendic C, figure C.3. This visualizes how the suspensions look and helps in understanding how the suspension is structured.

2.3 Transport of electrons and electro-active particles

2.3.1 Ion flux: Nernst-Planck equation

Within an electrode, the flux of a charged chemical species i can be described by the Nernst-Planck equation [2]:

$$\vec{N_i} = -z_i u_i F c_i \nabla\Phi_2 - D_i \nabla c_i + c_i \vec{v}. \tag{2.8}$$

The Nernst-Planck equation summarizes the species movement due to migration, diffusion and convection. The first term after the equal sign denotes the migration, which represents the motion that results from a potential gradient. It consists of the valence z_i, the mobility u_i [m^2 V^{-1} s^{-1}] (which is the ability of charged particles to move through a medium under the influence of an electric field or potential gradient), the Faraday constant F = 96485.33 s A mol^{-1}, the concentration of the species c_i [mol cm^{-3}] and the potential gradient [V m^{-1}] over a flow cell. The second term relates the diffusive flux to the concentration gradient with D_i [m^2 s^{-1}] the diffusion coefficient of a species in a specific electrolyte and the concentration gradient ∇c_i [mol m^{-4}]. The third term is a convective term and represents the motion of the species by local velocities of the fluid, with the velocity v in [m s^{-1}] of the fluid. This will give a flux of species in [mol m^{-2} s^{-1}].
The main goal is to develop an understanding of the behaviour of active species of a flowing SSFB suspension. Looking at the system in three dimensions is beyond the scope of the project. The focus will be to look at the behaviour of the active species in the plane determined by the current collector and the membrane.
The following sections will discuss the different terms of the Nernst-Planck equation in more detail.

2.3.2 Velocity profile in a flow cell

The convective term can be determined by looking at the velocity profile that develops in the flow cell when a fluid reaches a stationary laminar flow. For the determination of the velocity profile in a flow cell, the start is to draw up a force balance over a small volume in the flow cell. The assumption is that the suspension entered the cell and reached a fully developed laminar flow. From the perspective of a control volume, there multiple forces act on it. [12] A schematic representation of the forces acting on the control volume can be found in figure 2.3.
The control volume is taken over a distance dx and height dy. Pressure forces, shear forces and gravity act on the volume. P_x denotes the pressure on the volume at x, P_{x+dx} denotes the pressure on the volume at $x + dx$. On y and $y + dy$, shear stress τ_y and τ_{y+dy} respectively act along the surface of a layer of fluid with thickness dy. The notation of $\tau_{i,j}$ says that at location j along the length of the cell, the stress acts on a fluid layer at height i. τ is defined as the shear stress the surroundings exert on

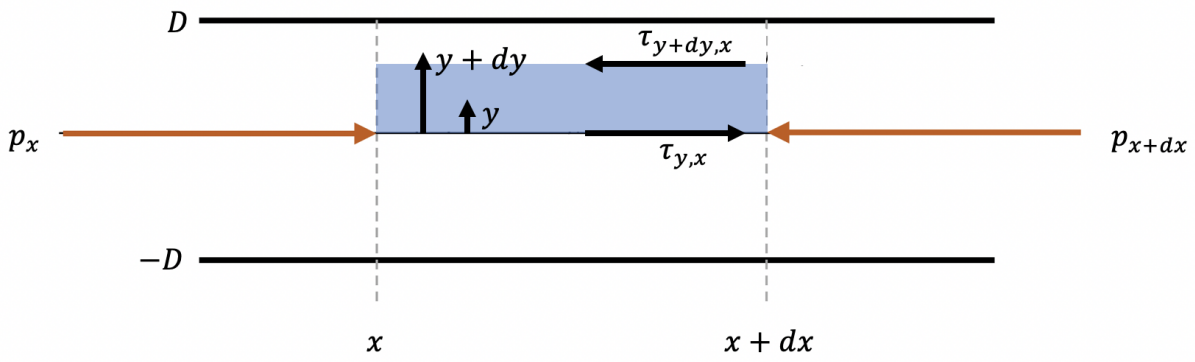

Figure 2.3: A schematic representation of the forces acting on a finite control volume (light blue) with thickness dy in a flow cell. x denotes the horizontal distance, y denotes the height of the flow cell. The different forces are discussed below.

the control volume. On y, the force acting on the control volume is positive, for it is the adjacent layer working on the control volume. With the same reasoning, on $y + dy$, the force acting the control volume is negative. So, at y, τ_y is in the positive direction and at y τ_{y+dy} in the negative direction. The total force balance on the control volume is found to be:

$$0 = -\rho dx dy B g_x + P_x dy B - P_{x+dx} dy B + \tau_{y,x} dx B - \tau_{y+dy,x} dx B \tag{2.9}$$

in which the density of the fluid is represented by ρ, the depth of the control volume by B and the gravity by g. Because the flow cell is horizontal in this case, the gravitational factor drops out and by dividing the force balance by the control volume $dxdyB$, the following expression is found:

$$0 = \frac{P_x - P_{x+dx}}{dx} + \frac{\tau_{y,x} - \tau_{y+dy,x}}{dy} \tag{2.10}$$

which leads to

$$\frac{d\tau_{y,x}}{dy} = \frac{\tau(y+dy) - \tau(y)}{dy} = -\frac{P(x+dx) - P(x)}{dx} = \frac{dP}{dx}. \tag{2.11}$$

The pressure drop over the flow cell over a length dx is constant, which is why the expression can be expanded to the following:

$$\tau_{yx} = -\frac{\Delta P}{L} y + C_1 \tag{2.12}$$

with ΔP the pressure drop over the entire length of the flow cell and C_1 an integration constant. In the center of the flow cell at $y = \frac{1}{2}D$, in a cell that starts at $y = 0$ and ends at $y = D$, the shear stress is zero, for the velocity is maximum. Together with the expression for the shear stress for non-Newtonian fluids given by equation 2.7, an expression for the velocity gradient (or shear rate) can be found. Equation 2.13 shows the result.

$$\frac{\Delta P}{L}(y - \frac{1}{2}D) = -\eta_{app}(\dot{\gamma}) \frac{du_x(y)}{dy} \tag{2.13}$$

$\eta_{app}(\dot{\gamma})$ denotes the apparent viscosity as defined is equation 2.6 given in [Pa s] and $u_x(y)$ denotes the velocity of the fluid in x-direction at height y. In determining the velocity profile from $\dot{\gamma}$, the no-slip condition can be used. The no-slip condition for (viscous) fluids assumes that the fluid will have zero velocity relative to the boundary of the flow cell.

2.3.3 Current by ions and electrons

Battery capacity is a measure of the charge stored by the battery and it is determined by the mass of active material in the battery. It represents the maximum amount of energy that can be extracted from the battery under specific conditions. The theoretical possible capacity for an electroactive material can

be calculated with the C-rate. The C-rate indicates the time it takes for a battery to fully charge or discharge. Its unit is h^{-1} and the rate works as follows. A battery having a C-rate of 2 can be charged in half an hour, while a C-rate of $\frac{1}{10}$ means the charging process takes 10 hours. The theoretical capacity in [A · s g^{-1}] can be calculated by the following:

$$Q = \frac{F}{M_w \times 3.6} \tag{2.14}$$

in which F denotes the Faraday constant (96485.33 s A mol^{-1}) and M_w is the molar mass in g mol^{-1} of a molecule of electroactive material. The molar mass of $Li_4Ti_5O_{12}$ is 459.1 g mol^{-1} and Q is therefore equal to Q = 58.38 mA h g^{-1}. Noted is that this a theoretical value of the capacity under optimal circumstances. There are processes known that lead to capacity loss in the battery: Li^+ deposition, electrolyte decomposition, active material clustering and passive film formation on current collector surfaces [21]. These processes will not be taken into account for this work. With the theoretical capacity, the current can be calculated as follows:

$$I = Q \cdot M \cdot C \tag{2.15}$$

in which I is the current, M is the mass of the electroactive particle and C the desired C-rate. Since the flow cell itself is electrically neutral, the current for both the electrons and the ions is equal, meaning that $I = I_{el} = I_{ion}$. The flow of ions and the current it carries can intuitively be compared to that of electrons. Electronic current means electrons push each other forward through a wire. In the flow cell, similar behaviour for ions for transport of ionic current occurs. The ions push each forwards, creating an ionic current.
The calculation of the current in the system can be used in the determination of the migration term in the Nernst-Planck equation. As will be explained in the next section, with both the current and the resistance in the system, the potential gradient can be calculated.

2.3.4 Resistance and potential gradient in a flow cell

The migration term of the Nernst-Planck equation contains a potential gradient, which is the rate of change of the potential over a displacement. As mentioned, both the current and resistance in the flow cell are needed in order to calculate it. The electronic and ionic resistances in the flow cell will be discussed below.
The electroactive particles and electrons experience a resistance while moving to the membrane and current collector respectively. A schematic overview of the movement of particles and the definition of the potential gradients are shown in figure 2.4.

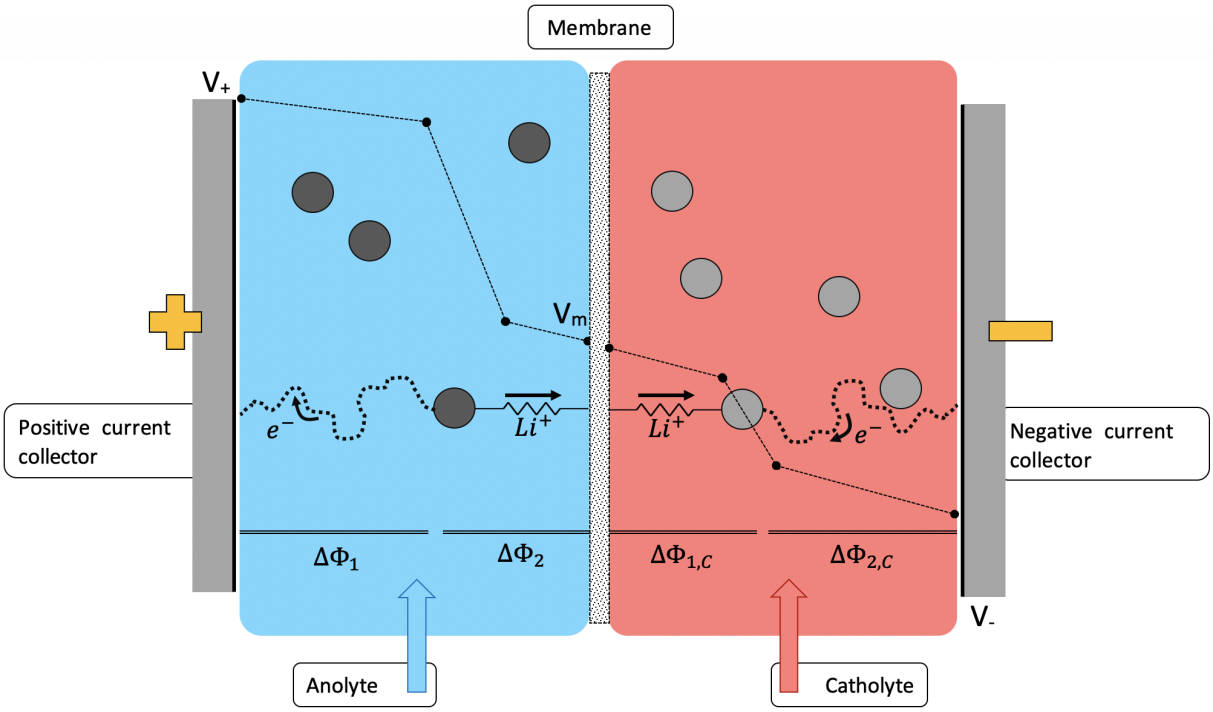

Figure 2.4: An overview of the movement of important particles in an SSFB flow cell. The dark circles represent active species in the anolyte, while the lighter circles in the catholyte denote the other species needed for the redox reaction. As can be seen, the electrons e^- follow a network, formed by CB particles (see also figure 2.1). The resistance for Li^+ is more discussed in the text of section 2.3.4. The dashed line represents a possible potential drop over the different regions of resistance and $\nabla\Phi_1$ and $\nabla\Phi_2$ represent the electronic (1) and the ionic (2) potential gradient and the index C stands for *catholyte*.

Of special interest is the different sections the potential drop can be divided in. There is a region with electronic resistance where the potential drops, denoted as the section with the two horizontal lines and $\nabla\Phi_1$ underneath in figure 2.4. The second region denotes the resistance of and around the active particle. The third region is due to the resistance of a Li^+-ion in the fluid medium and near the membrane, denoted with a resistance symbol in figure 2.4.
A schematic representation of the different contributions to the electronic and ionic resistance is given in figure 2.5.

The electronic resistance denoted by $R_{electronic}$ is determined by the conductivity σ of the CB network, being a function of the velocity profile. The following three resistances stand for the internal ionic resistance. It consists of $R_{internal}$, the resistance the Li^+ experiences in the active particle while Li^+ is separated from in the redox reaction (in other words, the resistance of the reaction kinetics). It also consists of R_{gel} and of $R_{boundary}$. R_{gel} stands for gel-like layer around the active species formed by polymers that are a consequence of chemical reactions of the electrolyte with the dissolved salt and the surface of the active species. The formation of this layer is also called solid-electrolyte interface (SEI) formation [4] [13]. $R_{boundary}$ in this set represents the resistance that arises from the fluid medium flowing around the species. Because of their individual complexity, these three resistances internal ionic resistance are treated as being one resistance.
The next three resistances in figure 2.5 are treated as one resistance term as well: the external ionic resistance. It consists of the resistance Li^+ encounters (due conduction through the medium as well as by convection and diffusion) as it moves through the fluid medium, $R_{ion,fluid}$, a fluid boundary layer resistance along the membrane, similar to the fluid boundary layer around the active species, with $R_{boundary}$ belonging to this phenomenon as well. The following resistance is a resistance occurring at the electrolyte—membrane interface $R_{e|m,interface}$ as Li^+-ions dissolve into the membrane. This resistance for example depends on the willingness of the membrane to absorb ions. In appendix B, a simulation for the ion flux at this electrolyte—membrane interface can be found.
With Ohm's law and inserting the resistance and current, the potential drop over each consecutive section

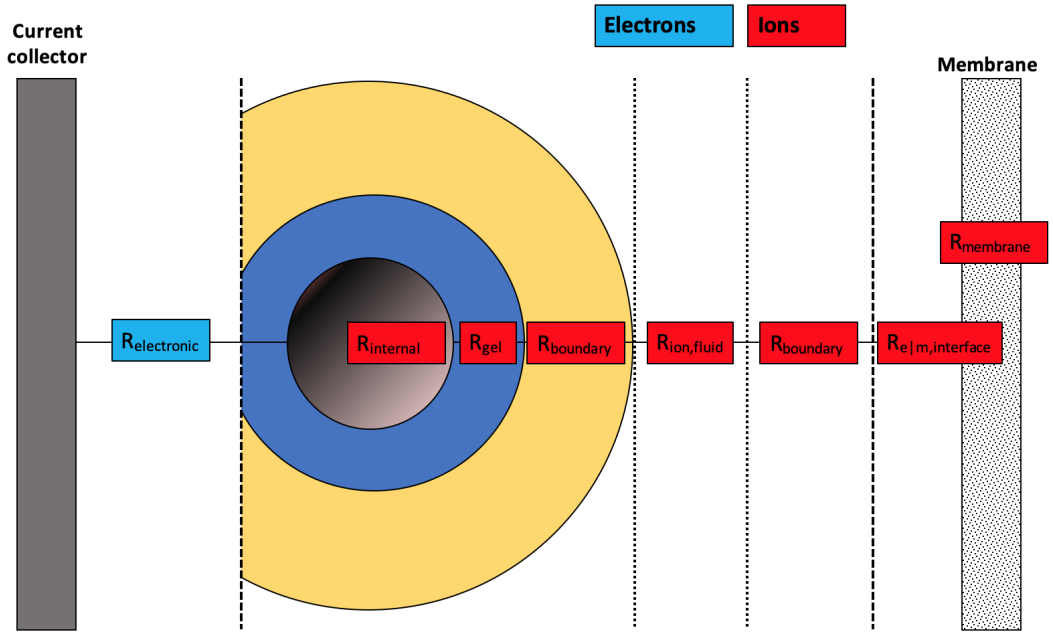

Figure 2.5: An overview of the different contributions to the resistance in a flow cell. The blue rectangle denotes electronic resistance and the red rectangles represent the different ionic resistances. The dark circle, blue circle and yellow circle represent the active species, gel layer and fluid boundary layer around the species.

can be determined. The potential gradient is defined as follows:

$$\nabla \Phi_k = \frac{dV_k}{dy} \tag{2.16}$$

and has units [V m^{-1}]. k stands for the particle for which the potential gradient is determined, as a distinction is made between electrons and ions. The electronic potential gradient is indicated by $\nabla \Phi_1$ and the ionic potential gradient is indicated by $\nabla \Phi_2$.

2.3.5 Diffusion electro-active material

Due to the high concentration of Li^+ in the flow cell, the concentration in the bulk of the flow cell in this report is treated to be constant. This leaves the following for the diffusive term:

$$\nabla \, c_i = 0.$$

This means diffusion will not be considered in the bulk in this report. Diffusion plays a prominent role, however, for ions at the boundary layers in this system. In the bulk of the flowing suspension migration and convection are the significant factors contributing to the ion flux.

3 Experimental Method

The goal of this chapter is to explain what methods are used to determine the resistances and the ion flux in SSFB cells. The models with which the different contributions to the Nernst-Planck equation are determined are one-dimensional and will look at the ion flux in the direction perpendicular to the bulk flow direction of the suspensions through the flow cell. For the ion flux, the positive flux direction is taken to be in the direction of the membrane in between the battery flow cell, looking from the current collector. The potential difference that would occur if two half-cells with a membrane in between would be used is simulated by placing a potential over the flow cell. In the case of the papers used, this will lead to a model that uses data of a battery in discharge. The calculations are performed in MATLAB [27].
Viscosity measurements for Duduta et al. (2011) were performed using a Brookfield controlled shear-rate viscometer (Model RVDV-II + Pro, Brookfield Engineering, Middleboro, Massachusetts, USA). [13]
The rheological and electrical measurements for Youssry et al. (2013) and Madec et al. (2014) that gives the viscosity and conductivity data are done with a controlled rheometer (Physica MCR 101, Anton Paar) connected with a standard potentiostat/galvanostat (SP200 from Biologic). [16] [19]
In Appendix B, a method developed by Knehr et al. (2012) is used to determine the ion flux near the electrolyte—membrane interface. The method used by Knehr et al. (2012) is different from the methods discussed below, which is the reason that it is treated separately.

3.1 Velocity profile calculation

Given that the Nernst-Plack equation can be split into multiple sections which can be calculated seperately, the first goal is to determine the velocity profile for multiple types of suspensions that can be used for the SSFB. As discussed in section 2.3.2, the velocity of a system under flow in a cell can be found from the apparent viscosity η_{app} and the shear rate $\dot{\gamma}$. In order to determine the velocity profile from these quantities, each measured $\dot{\gamma}$ must be linked to a certain height in the flow cell so that $u_x(y)$ can be determined.

The expression for the shear rate will be restated here:

$$\dot{\gamma} = \frac{du_x}{dy} = -\frac{1}{\eta_{app}(\dot{\gamma})}\frac{\Delta P}{L}(y_i - \frac{D}{2}). \tag{3.1}$$

Since the apparent viscosity is a function of the shear rate, this equation must be solved numerically to find $\dot{\gamma}$ at each corresponding height y_i in the flow cell. The height of the flow cell will be discretized and via an iteration scheme the $\dot{\gamma}$ and each height y will be found. A slightly adjusted version of Eq. 3.2 is shown next to show how the iterating equation looks like.

$$\dot{\gamma}_{k+1} = -\frac{1}{\eta_{app}(\dot{\gamma}_k)}\frac{\Delta P}{L}(y_i - \frac{D}{2}) \tag{3.2}$$

For each value of y_i, a value for $\dot{\gamma}$ will be estimated. The corresponding value of $\eta_{app}(\dot{\gamma})$ from a data set of the papers at that $\dot{\gamma}$ is inserted in Eq. 3.2, which will give a new value for $\dot{\gamma}$. For this $\dot{\gamma}$, a η_{app} is found in the data, which again is inserted in Eq. 3.2. This process will continue until iteration converges and the value of $\dot{\gamma}$ is non-changing permanently. The found value of the shear rate is the value that belongs to the inserted y_i. This process is repeated until the entire shear rate profile over the flow cell height is calculated.

The shear rate can be calculated from the velocity, but this also be done the other way around. From $\dot{\gamma} = \frac{du_x}{dy}$, solving for u_x means an integral over the height of the flow cell must be solved. But as this must be solved numerically, the the height is discretized. The velocity profile is thus calculated using the following sum:

$$u_x(y) = \sum_{i=0}^{D} \dot{\gamma}_i \Delta y.$$

With D the height of the flow cell and Δy the spacing between each subsequent y_i. In order to minimize the error produced by using Δy instead of an integral with infinitesimal spacing, the summation is worked out until half the height of the flow cell, $D/2$, and the result is mirrored around the center. The velocity profile of a laminar flowing medium in a tube is symmetric in the center, which therefore

validates this way of treating the summation. The velocity profile in the flow cell of a SSFB suspension should look similar to the velocity profile shown in figure 3.1. The entire height of the flow cell is indicated in the figure with y. For the remainder of this report, the membrane in the flow cell is at $y = 0$ mm and the current collector at $y = 1.4$ mm, similar to the flow cell dimensions used in Duduta et al. (2011) and Youssry et al. (2013) and Madec et al. (2014), and the focus will be on the flux behaviour in one half cell of the SSFB.

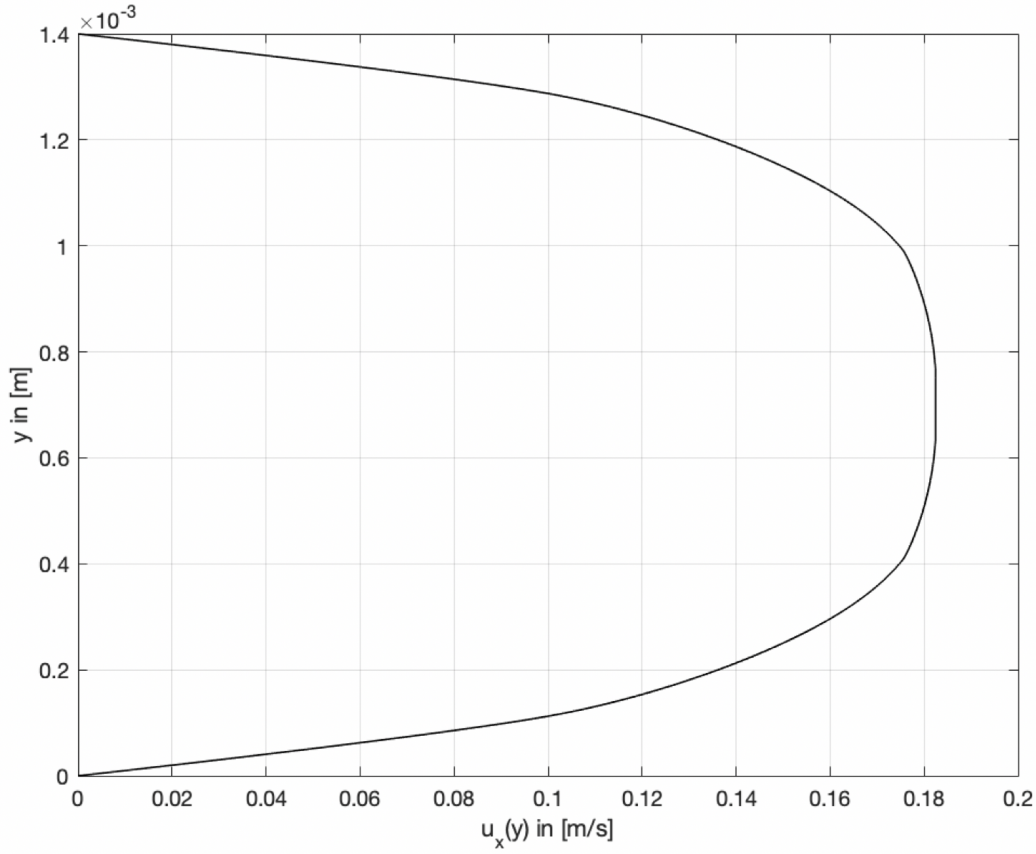

Figure 3.1: The velocity profile of a suspension in a Semi-Solid Flow cell. y denotes the height in the flow cell, $u_x(y)$ the velocity of the suspension at each corresponding height y. Data is used from Youssry et al., figure 8, $\phi_{KB} = 0.021$ [19].

For every suspension that is treated, the velocity profile will be calculated and later inserted in equation 2.8. The data that is required to find the velocity profiles will be extracted from Youssry et al. (2013) [19], from Duduta et al. (2011) [13] and from Madec et al. [16] using WebPlotDigitizer [24]. Youssry et al. (2013) contains viscosity and conductivity data for different volume fractions and types of carbon black particles in SSFB suspensions, Duduta et al. (2011) contains viscosity data at differing shear rates for different types of suspensions and Madec et al. (2014) contains viscosity and conductivity data for different types of suspensions at different shear rates. The Youssry et al. (2013) data and the Duduta et al. (2011) data will be used to develop a model base that can be used to evaluate data from Madec et al. (2014).

The viscosity data that is used can be found under section 4.1.

3.2 Electronic conductivity profile determination

In order to develop results about the potential gradient profile over the flow cell needed in equation 2.8, the current and electronic resistance in the flow cell must be determined. With Ohm's law, the potential gradient can be calculated from these two quantities. If the resistance in the flow cell at each consecutive height is known, the full resistance profile can be formed and used to continue the calculations. The electronic conductivity profile in a flow cell can be determined from data where the

conductivity is measured for different shear rates in a flow cell. Since the shear rate can be calculated from the velocity with:

$$\dot{\gamma} = \frac{du_x}{dy},$$

a link can be made with figure 3.1 to see how the shear rate will evolve over the height of the flow cell. The shear rate is calculated from the difference in velocity over a height dy. The more the velocity changes over that dy, the larger the shear rate. Compared to figure 3.1, it becomes clear that the shear rate in the middle of the flow cell is equal to zero and highest at the edges. Keeping this relation in mind while determining the conductivity profile reveals what types of CB agglomerations are present around every height in the flow cell.

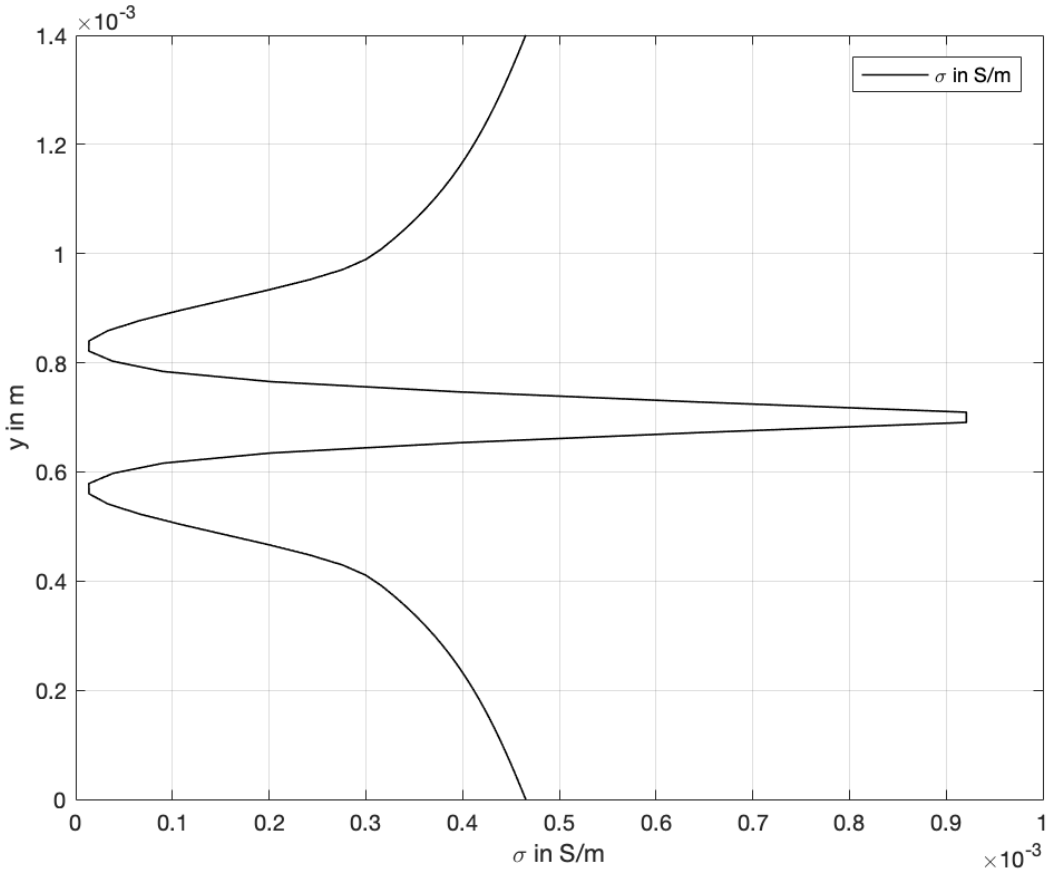

Figure 3.2: The conductivity profile of a suspension in a flow cell with Ketjen Black volume fraction $\phi_{KB} = 0.021$. y denotes the height in the flow cell, σ the conductivity of the suspension at each corresponding height y. Data is used from Youssry et al. [19].

Similar to the extraction of viscosity data in the previous section, the conductivity data for different suspensions in the used papers is determined using WebPlotDigitizer [24]. The data is interpolated and fitted in order to get a finer data structure. Since it is known that the velocity of the suspension in a flow cell is highest in the center, this is where the shear rate will be lowest. The conductivity data is pasted in a flow cell starting from the center to either of the two edges and mirrored around the midline.
The validation of presenting the conductivity this way lies in the symmetry of the velocity profile of a flowing suspension in the flow cell. The symmetry holds when switching to the shear rate, for it is calculated from the velocity. Since the conductivity is dependent on shear rate, it too can be mirrored around the center.
The electronic conductivity profile in the flow cell of a SSFB suspension is expected to have a similar complex pattern as the example profile shown in figure 3.2.

3.3 Resistance and potential drop determination

With the electronic conductivity profile over the height of the flow cell, the first step is made in calculating the potential profile over a SSFB flow cell. The following step is to calculate the electronic resistance from the electronic conductivity. Figure 3.3 is used as a model to determine what this resistance should be.

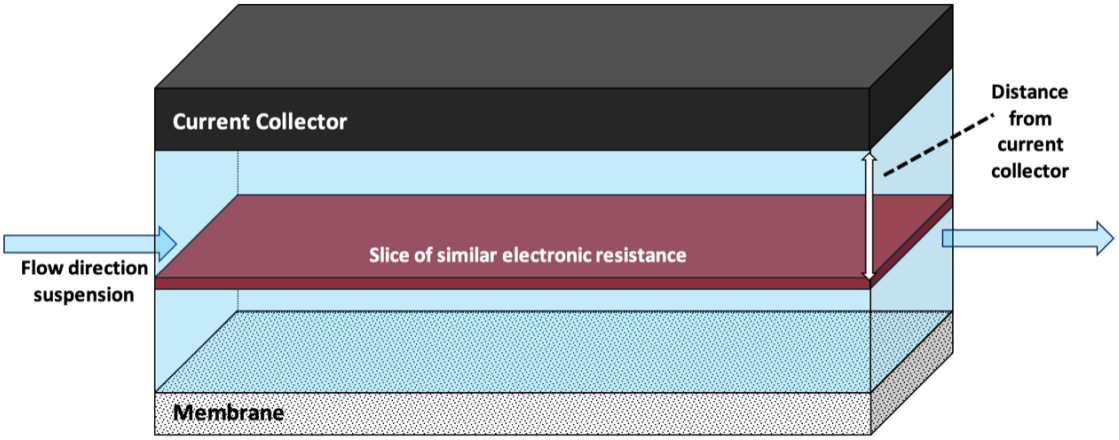

Figure 3.3: Overview of how the flow cell will be subdivided in order to calculate the electronic resistance from the conductivity data. The current collector is denoted is dark grey, the suspension in transparent blue, the membrane as a dotted surface and the resistance slide is indicated in red. The white arrow indicates what is meant by the distance of the slice from the current collector.

In the determination of the resistance, we subdivide the flow cell in slices that are assumed to have equal conductivity. The surface of the slice is considered to be filled with LTO particles entirely. However, since the particles are treated to be spherical, the assumption that the entire surface is covered with LTO particles is not fully correct. There will be some space between each consecutive particle due to its spherical geometry, because the areas of the intersections (a circle) of each of the spheres are not able to fully cover the rectangular surface.
Electrons originating from the redox reactions are not solely produced near the current collector, but throughout the medium. For this report, it is assumed that the electronic flux towards the current collector is the same for all y.
Starting from the basic structure given by the model visualized in figure 3.3, the resistance in the flow cell can be found. The usual way of calculating the resistance from the conductivity is given by the following expression:

$$R = \frac{L}{A\sigma} \tag{3.3}$$

in which R is the resistance in [Ω], L is the length over which the resistance is taken, A is the surface through which current runs and σ is the conductivity in [S m^{-1}]. The surface is determined by the length and the width of the flow cell.
In order to determine the electronic resistance in the system with equation 3.3, it must be rewritten in order to account for the variable $\sigma(y)$. Rewrite equation 3.3 to infinitely small slices dy as

$$R \cdot A = \frac{1}{\sigma(y)} L \longrightarrow dR \cdot A = \frac{1}{\sigma(y)} dy \tag{3.4}$$

where σ is a function of the height y. Ohm's law can be written in terms of dR with

$$dV = I \cdot dR \tag{3.5}$$

the resistance can be found in the flow cell. Equation 3.4 and equation 3.5 are combined to find

$$dV = \frac{I}{\sigma(y)A} dy \longrightarrow V_y = \frac{I}{A} \int_0^y \frac{1}{\sigma(y)} dy' + V_0 \tag{3.6}$$

in which y' is a dummy variable to replace y in the integral and V_0 the starting value of V, which is zero as the only potential in the system is the potential as it is set over the flow cell externally. From equation 3.5 and the integral in the equations in (3.6) the total resistance over the entire height of the flow cell becomes

$$R_y = \int_0^y dR = \frac{1}{A}\int_0^y \frac{1}{\sigma(y)}dy' \longrightarrow R_y \cdot A = \int_0^y \frac{1}{\sigma(y)}dy'. \tag{3.7}$$

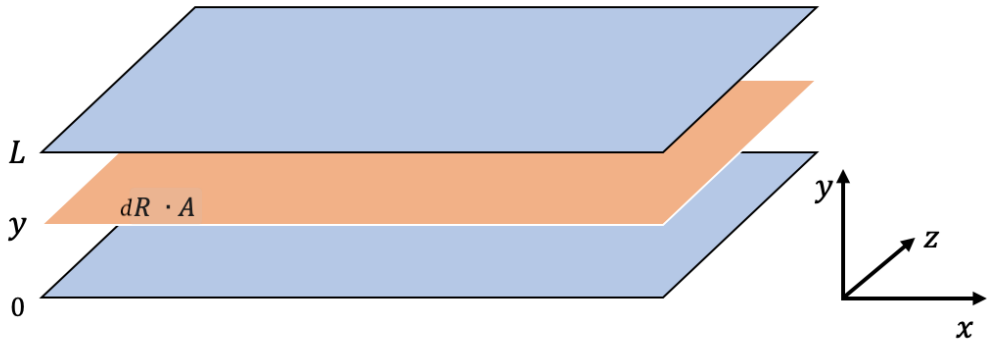

Figure 3.4: A schematic overview of how the electronic resistance in the system is treated. The height of the flow cell is given as y and it runs from 0 to L. The orange slab represents the $R_y \cdot A$ that is calculated in equation 3.7.

Since the resistance is calculated between parallel plates, it is clear from equation 3.3 that when $A \to \infty$, $R \to 0$. To eventually have a resistance that is meaningful, the surface and resistance must be treated as in equation 3.7. This gives the opportunity of calculating the electronic resistance in $[\Omega \cdot m^2]$ over a certain height in the flow cell. The resistance of an electron flowing through the flow cell exists for it has to move through the carbon network.
Once the electronic resistance over certain distances from the current collector is known, the potential drop over that distances can be calculated using Ohm's law with the current calculated as in equation 2.15. The assumption made here is that the electrons run in a straight line to the current collector. In reality, the carbon network will form strings of irregular shape through which the electrons are transported. Next to that is the releasing of electrons - not all electrons are released at the same height y. However, the integral in equation 3.7 can be evaluated from y =0 to a certain height y. This way, it can be calculated what the resistance is an electron experiences when travelling to the current collector when it is released at a certain height y. The potential difference (over dy) is calculated with:

$$d\Phi_1(y) = dR(y) \cdot I_{el} \tag{3.8}$$

in which $d\Phi_1$ stands for the potential drop by the electronic network, similar to how a general dV due to a resistance is calculated in equation 3.5. The notation $d\Phi_1$ is used in preparation to when the potential gradient will be calculated, which has notation $\nabla\Phi$. However, as the electronic resistance is calculated in units of $[\Omega \cdot m^2]$, the calculation to find the potential drop from Ohm's law must be carried out with a current density I" in $[A \cdot m^{-2}]$ instead the current in $[A]$ in order to find the potential in units of $[V]$. The current density can be found be making an geometrical assumption about the flow cell and what value will be of the area the current will flow through. The orange surface in figure 3.4 is the surface that is meant. The length of a flow cell as used in Duduta et al. (2011) and in Youssry et al. (2013) had a value of $L = 80$ mm and a height and a width of 1.4 mm. The surface A is then calculated to be 112 mm^2. The current density can be found by first calculating the estimated current in the system using equation 2.3.3 and then inserting it in the following equation:

$$I" \cdot A = \frac{dV}{R} \longrightarrow I" = \frac{dV}{R \cdot A} \tag{3.9}$$

where it is assumed that I" will be constant over the height of the flow cell. It has units $[A \cdot m^{-2}]$.

With equation 3.7, the electronic resistance can be calculated. Together with the current density already determined by equation 3.9, the contribution of the electrons to the potential drop can be calculated:

$$d\Phi_1 = I" \cdot dR(y). \tag{3.10}$$

A potential over a flow cell is set, $V(y = L) - V(y = 0)$, noted as $d\Phi_{tot}$ in [V]. With $d\Phi_1$ calculated, this leaves the remaining of the total potential drop $d\Phi_{tot}$ to the ionic resistances in the system. From the conductivity of Li^+ in propylene carbonate electrolyte [25], the contribution to the potential drop from the ions in the fluid medium can be determined using a similar method as for the calculation of the eletronic resistance (but this time, the travelled path is from a certain height y in the flow cell to the membrane instead of to the current collector). Every layer of dy has a conductivity σ_{Li} specific for the ions in the electrolyte. However, this σ_{Li} does not depend on the shear rate, as the electronic conductivity does (see figure 3.2 for example). This means that the ionic conductivity will increase in fixed steps from the membrane up to the current collector. The potential drop that arises from the ionic resistance in the electrolyte and the electrolyte—membrane interface is denoted with $d\Phi_{ext,ionic}$ and is determined in similar fashion as for the electrons. This leaves only the determination of the potential drop over the electroactive species, or $d\Phi_{int,ionic}$. The potential drop over the electroactive material (originating from $R_{internal}$, figure 2.5) is determined by:

$$d\Phi_{int,ionic} = d\Phi_{tot} - d\Phi_1(y_1) - d\Phi_{ext,ionic}(y_{ext,ionic}). \tag{3.11}$$

The electronic resistance and external ionic resistance are determined with equation 3.7. For electrons the integral for $R(y) \cdot A$ starts at the current collector, for the ions it starts at the membrane. In runs until a height y within the range of 0 mm to 1.4 mm (y_1 for electrons, $y_{ext,ionic}$ for ions). This means that the resistance an electron or ion experiences from that height y_1 to the current collector or $y_{ext,ionic}$ membrane respectively can be calculated. Multiplying either of these resistances with the current density $I"$ found by using equation 3.9 gives the potential drop by either the electronic resistance and the ionic resistance over the height y_1 and $y_{ext,ionic}$. That is what the $d\Phi_1(y)$ and $d\Phi_{ext,ionic}$ mean in 3.11.
The potential difference over the active species and the path the ions have to travel add up to

$$d\Phi_2 = d\Phi_{int,ionic} + d\Phi_{ext,ionic} \tag{3.12}$$

This way, the contributions of specifically the electrons and the ions to the potential drop can be determined.
The flow cell is electrically neutral, for the redox reaction releases an electron and a positively charged ion. With the electrical neutrality, the assumption can be made the the electronic current is equal to the ionic current. Otherwise, the flow cell would not be electrically neutral, so: $I"_{electronic} = I"_{ionic}$. This means that the calculated current in equation 3.9 is used to calculate both the electronic resistance and the external ionic resistance (with equations 3.7 and 3.13).
What should be noted here, is that from the potential differences due to electronic and ionic resistances, potential gradient profiles can be calculated. These are needed for the determination of the species flux as given in equation 2.8. The potential gradient profile is found as explained in the following section.

3.3.1 Potential gradient

As mentioned, the potential gradient is defined as the potential difference divided by the distance from the current collector or membrane (depending on the particle discussed). The expression is restated here:

$$\nabla\Phi_i(y) = -\frac{d\Phi_i}{dy} \tag{3.13}$$

where dy denotes the distance over which $d\Phi_i$ is taken. The electronic, internal ionic and external ionic potential gradient can all three be determined separately.

3.4 Active material flux

For completeness, the Nernst-Planck equation is shown again to discuss what is the final process in determining the ion flux in a flow cell.

$$\vec{N_i} = -z_i u_i F c_i \nabla \Phi_2 - D_i \nabla c_i + c_i \vec{v}$$

The focus is to work in a one-dimensional model, which means that the vectorial character of the ion flux can be disregarded. This leaves a one-dimensional ion flux through the height of the flow cell:

$$N_i = -z_i u_i F c_i \nabla \Phi_2 - D_i \nabla c_i + c_i v \tag{3.14}$$

As the concentration of the suspension in the bulk of the fluid is assumed to be evenly distributed, the diffusion term in the Nernst-Planck equation is taken to be 0. This leaves the migration and convection term that contribute to the ion flux. The valence z_i, mobility u_i, Faraday constant F and concentration c_i are either looked up or calculated. The ionic potential gradient is expected to remain (nearly) constant per suspension over the height of the flow cell, for it depends on the internal and external ionic resistances, which are properties of the electroactive material.
The results will be plotted in a bar graph which allows for a clear visualisation of the contributions to the ion flux.

3.4.1 Convection and migration ratio

The convection term is given by multiplying a local concentration of the suspension by the corresponding local velocity the direction of the length of the flow cell (x-direction, see figure 3.4). It is assumed that the concentration of Li^+-ions is relatively high, due to the presence of a great amount of electroactive material. As can for example be seen in the right graph of figure 4.5 (which is a graph that displays the electronic resistance as a function of the height y for $Li_4Ti_5O_{12}$ (LTO) calculated for semi-solid battery suspensions from Madec et al. (2014)), the typical weight percentage of the electroactive species lies between 15 wt% and 25 wt%.
Moreover, the suspension in a semi-solid flow battery is constantly refreshed by the pumps. Therefore, if flow rates and Li^+ concentrations are relatively high, the concentration is assumed to be constant over the length and height of the flow cell and the residence time relatively short.

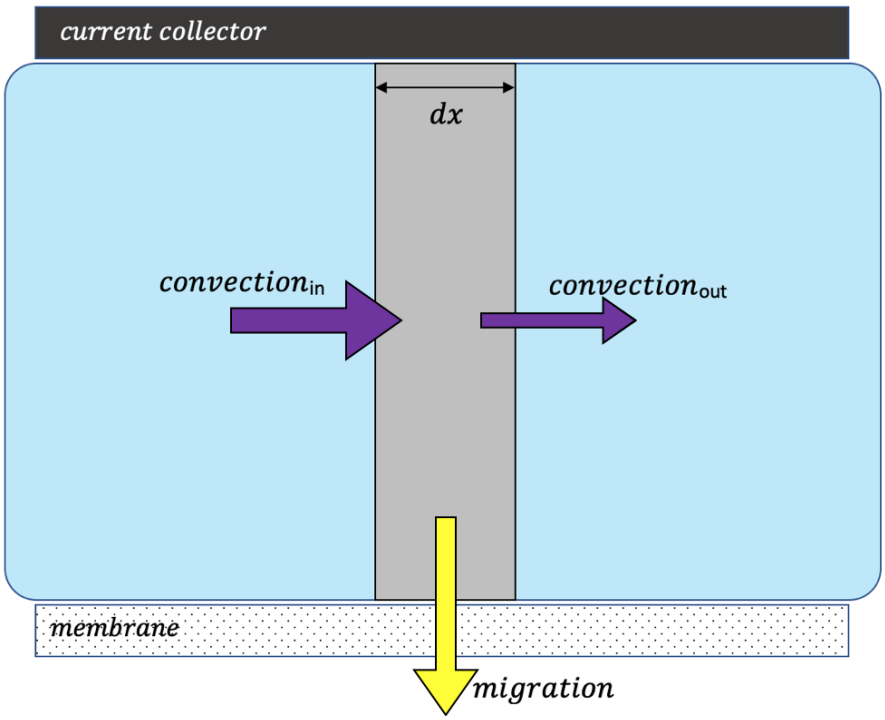

Figure 3.5: Representation of the fluxes in a slab of width dx in the flow cell. The purple arrows denote the flux by convection through the grey slab, and the yellow arrow pointing downwards represents the flux due to migration. The ionic migration will be towards the membrane, since the electrons will follow the carbon network towards the current collector.

The short residence time for suspensions is assumed from the velocity profiles of similar systems, such as the determination of the velocity profiles for $LiCoO_2$ (LCO) suspensions in Duduta et al. (2011) and velocity profiles calculated for suspensions used in Youssry et al. (2013) (for example figure 3.1). The corresponding velocity values in these profiles are of the order $0.01 - 0.1$ m s^{-1}, so the residence time in a flow cell of length of $L = 80$ mm [13] is relatively short.

The following will describe how the migration and convection of the suspension relate to each other, so that the order of magnitude of both terms can be determined. It is explained how the assumption of constant concentration along the x- and y-direction can be checked on its validity.
In figure 3.5, a small slab in the flow cell with a width of dx is drawn with three separate arrows that represent fluxes through the drawn slab. The total supply of the suspension is given by the convection in-flux and the flux that leaves the slab is represented by the convection out-flux. There will be migration of ions towards the membrane, the amount of which will be a fraction of the inwards flux by convection. To determine how large this fraction will be, the following ratio will be used (with the use of the migration and convection expressions in equation 2.8):

$$\varphi = \frac{migration}{convection} = \frac{\mid -z_i u_i F c_i \nabla \Phi_2 \mid}{\mid c_i \langle v_x \rangle \mid} = \frac{z_i u_i F \mid \nabla \Phi_2 \mid}{\mid \langle v_x \rangle \mid} \tag{3.15}$$

in which φ is called the Rohde ratio. Its value says what fraction of in-flux by convection in a slab of width dx leaks away by migration. When its value is much smaller than 1, little of the convection in-flux flows away due to migration. If φ is equal to 1, the total in-flux by convection leaks away due to migration towards the membrane. When φ is in between these two cases, a substantial fraction of convection leaks away. Only when $\varphi \ll 1$ is the assumption that the concentration in the flow cell is constant valid. If φ is in between being much small than 1 and equal to 1, an intermediate value, then a considerable amount of the convection in-flux leaks away, meaning the concentration cannot stay constant.

This concludes the experimental method section. In this chapter, it was explained how the different contributions to the species transport in the Nernst Planck equation (2.8) will be calculated. The velocity profile is determined from viscosity—shear rate data for different suspensions and the potential profiles are calculated from the conductivity—shear rate data for different suspensions.

4.1 Convection (velocity profile)

In this section, the velocity profiles of different types of suspensions will be shown. The different suspensions contain two types of electroactive material: LCO or LTO. The carbon additives also vary in quantity. This section will thus look into how the different concentrations and materials used influence the velocity profile in a SSFB flow cell.
The first data set that is considered to develop the model is the data from Youssry et al. (2013) in which both the rheological and the electrical behaviour of non-aqueous carbon-black suspensions for lithium-based redox flow batteries are studied. The research has been done on suspensions containing either Ketjen Black or C45 carbon additives. The viscosity at different shear rates plots determined in the paper are used to determine the velocity profile in a flow cell of a specific size. The height of the flow cell is taken to be 1.4 mm with a length of $L = 80$ mm, with a pressure drop over the flow cell equal to $\Delta P = 7.5 \cdot 10^3$ Pa. [13] [19] The KB suspension velocity profiles can be found in figure 4.1 and figure 4.2. In figure 4.1, the $\phi_{KB} = 0.034$ data is not considered. The reason being that the scale of the found $\phi_{KB} = 0.034$ velocity profile is not in line with the other corresponding velocity profiles. This is due to the iteration scheme (explained in section 3.1) and amount of data points used per suspension data in the left graph of figure 4.1. The Discussion section will look more into why the $\phi_{KB} = 0.034$ velocity profile data set deviated so strongly compared to the other three velocity profiles in figure 4.1.

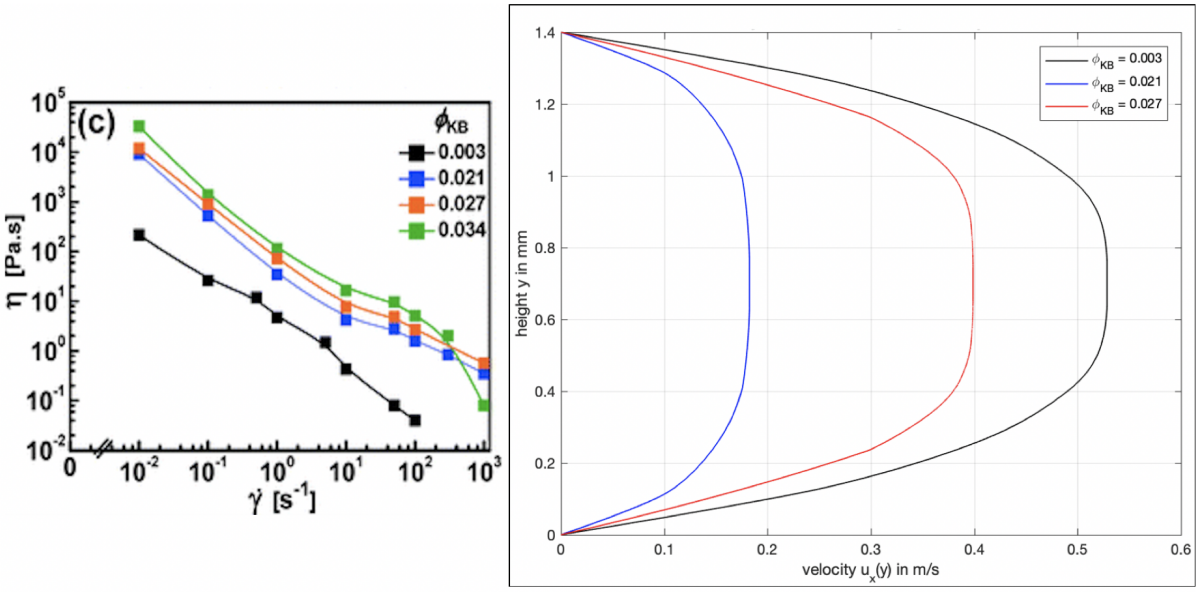

Figure 4.1: The velocity profile of a KB suspension in a Semi-Solid Flow cell. Left: η denotes the measured apparent viscosity in $[Pa \cdot s]$ and $\dot{\gamma}$ represents the shear rate in $[s^{-1}]$. y denotes the height in the flow cell, $u_x(y)$ the velocity of the suspension at each corresponding height y. Data (left plot) is used from Youssry et al. [19], where the data $\phi_{KB} = 0.034$ is not considered. The pressure drop over the flow is taken to be $\Delta P = 7.5cdot10^3$ Pa.

Important to note is the difference of the rheological behaviour between KB and C45. C45 data indicates more energy is needed to push the suspension forward through the flow cell, due to a higher viscosity compared to suspensions containing KB. Ketjen Black is therefore the preferred choice for flow battery systems [19], which as well will be discussed in the Discussion section.

The second data set (from Duduta et al. (2011) reveals similar velocity profiles in figure 4.3. The viscosity is measured at different shear rates for suspensions containing different amounts of KB and LCO.
The velocity profiles calculated from the Duduta et al. (2011) data help developing an idea of the rheological behaviour that is to be expected in SSFB systems. The suspension containing $LiCoO_2$ alone is not

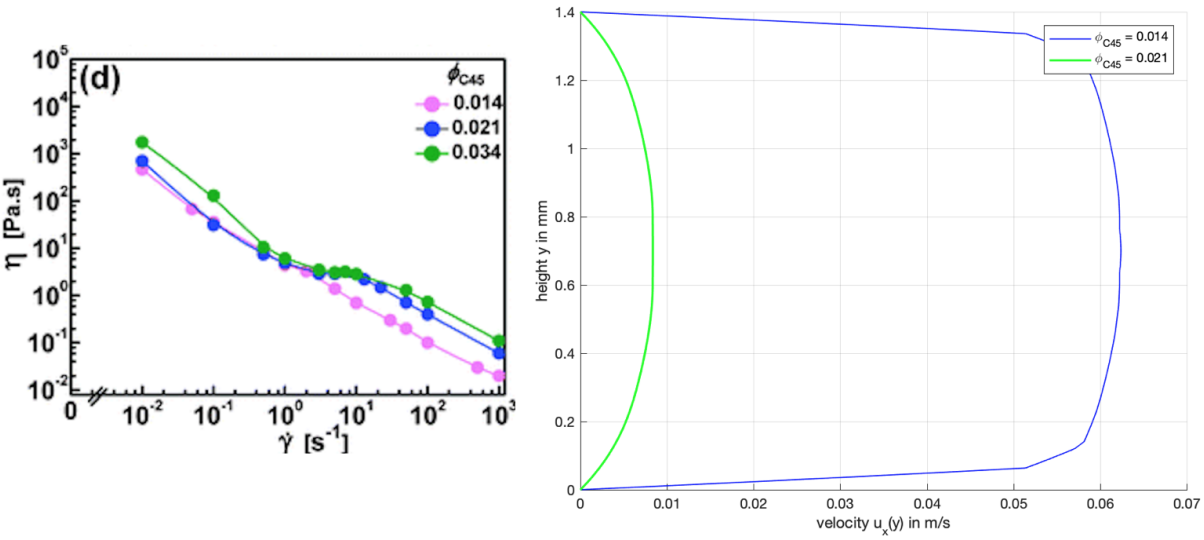

Figure 4.2: The velocity profile of a C45 suspension in a Semi-Solid Flow cell. Left: η denotes the measured viscosity in $[Pa \cdot s]$ and $\dot{\gamma}$ represents the shear rate in $[s^{-1}]$. y denotes the height in the flow cell, $u_x(y)$ the velocity of the suspension at each corresponding height y. Data (left plot) is used from Youssry et al. [19].

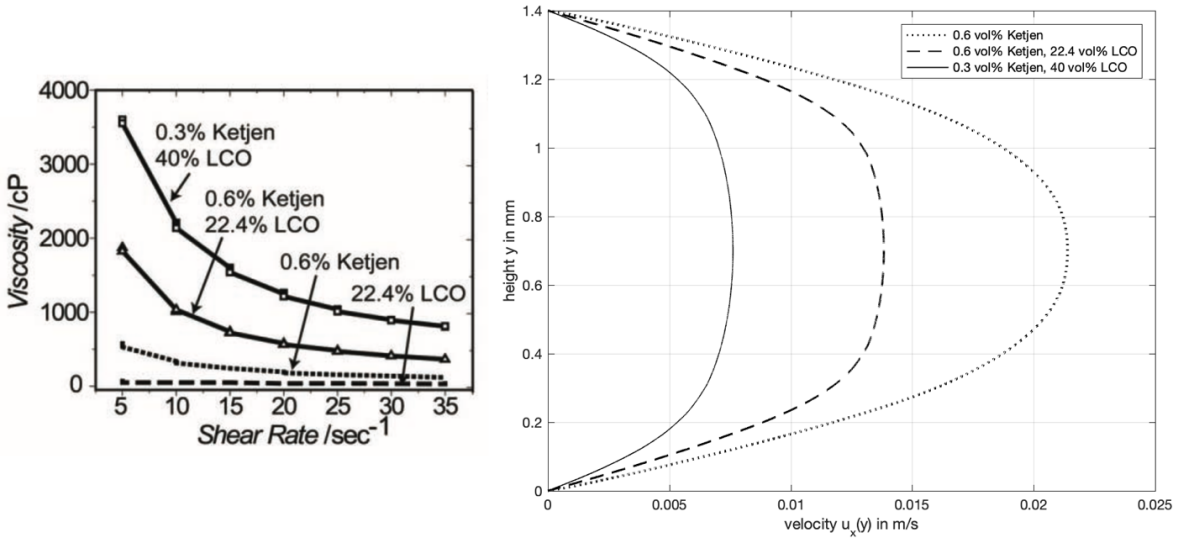

Figure 4.3: The velocity profile of a LCO-KB suspension in a Semi-Solid Flow cell. Left: η denotes the measured viscosity in $[Pa \cdot s]$and $\dot{\gamma}$ represents the shear rate in $[\frac{1}{s}]$. y denotes the height in the flow cell, $u_x(y)$ the velocity of the suspension at each corresponding height y. The dimensions of the flow cell are $y = 1.4$ mm, $L = 80$ mm and the pressure difference over the length of the flow cell is $\Delta P = 7.5 \cdot 10^3$ Pa. Viscosity data graph (left plot) is used from Duduta et al. [13].

considered, for it did not contain carbon black additives. The reason that the data from Duduta et al. (2011) is used to calculate velocity profiles, is that in Youssry et al. (2013) the viscosities of suspensions containing only Carbon Black particles are measured. In Duduta et al. (2011), the suspensions not only contain CB particles, but LCO electroactive material as well. This allows to first look into the rheological behaviour of CB, then a look into the rheological behaviour of suspensions with CB and electroactive material. From this, the influence on the rheological behaviour by adding electroactive material to the

SSFB suspensions can be seen.

The third data set that is considered is the set coming from Madec et al. (2014). The paper looked into both the rheological and the electrical behaviour of suspensions containing $Li_4Ti_5O_{12}$ (LTO) and Ketjen Black particles, both differing in weight percentage (wt%) in a 1M LiTFSI propelyne carbonate electrolyte. This means that from this paper, both the velocity profiles and potential profiles can be determined for SSFB suspensions. For the first two data sets, this could not be done, since Youssry et al. (2013) only looked into suspensions containing CB particles alone and Duduta et al. (2011) did not perform electrical measurements. These last two papers however help in developing an idea of what the rheological behaviour of SSFB suspensions looks like, providing a basis with which other rheological behaviour research can be compared with.

The final viscosity data set is extracted from Madec et al. (2014). The suspension contains $Li_4Ti_5O_{12}$ (LTO) and Ketjen Black particles, both differing in weight percentage (wt%) in a 1M LiTFSI propelyne carbonate electrolyte. One suspension contains carbon nanofibers (CNF) as well. For different shear rates, the viscosity and conductivity are measured in a flow cell of equal dimensions as Youssry et al. (2013) and the same pressure difference of $\Delta P = 7.5 \cdot 10^3$ Pa. The velocity profiles as a function of the height of the flow cell is determined and showed next to the viscosity data in figure 4.4.

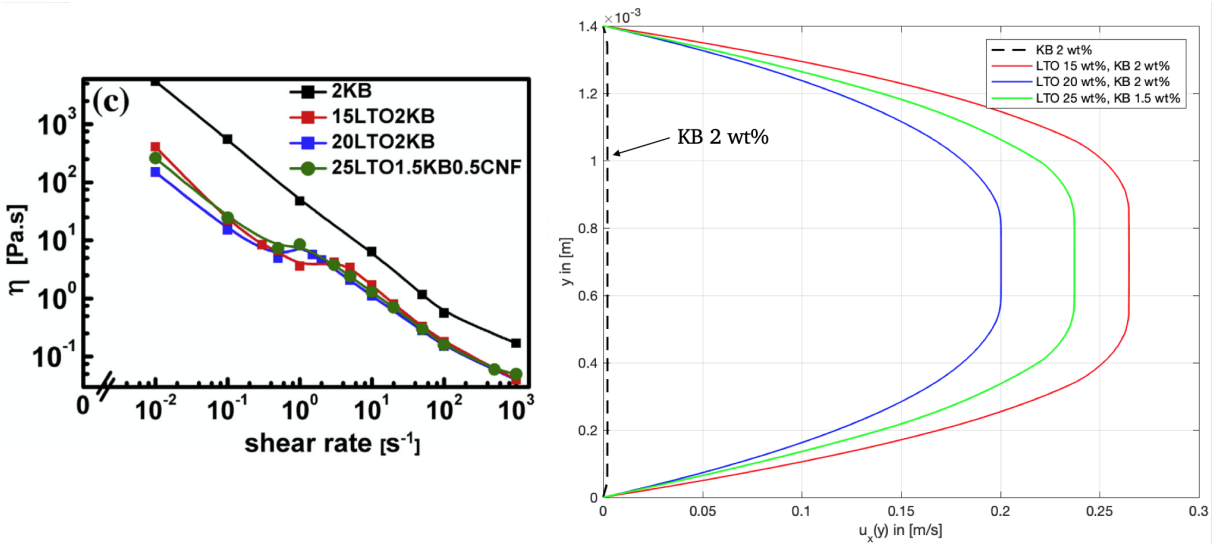

Figure 4.4: The velocity profile of a LTO-KB suspension in a Semi-Solid Flow cell. Left: η denotes the measured viscosity in $[Pa \cdot s]$and $\dot{\gamma}$ represents the shear rate in $[\frac{1}{s}]$. y denotes the height in the flow cell, $u_x(y)$ the velocity of the suspension at each corresponding height y. The dimensions of the flow cell are $y = 1.4$ mm, $L = 80$ mm and the pressure difference over the length of the flow cell is $\Delta P = 7.5 \cdot 10^3$ Pa. Viscosity data graph (left plot) is used from Madec et al. [16].

Notable is the significant difference in rheological behaviour between the suspension solely containing KB particles compared to the suspensions containing LTO and KB. The viscosity plot in figure 4.4 reveals the substantial increase in viscosity for the suspension with 2 wt% KB and no electroactive material. It is around twenty times higher than the other suspensions. The enhanced flowability of LTO-KB suspensions can be attributed to the dilution of the KB aggregates by the dispersed LTO particles, which weakens the tendency of the KB aggregates to form networks. [16]
Another interesting finding is that the 20LTO2KB suspension shows the lowest overall velocity profile, which means it is more resistant to flow than the suspensions with lower and higher LTO contents. As mentioned in section 2.2.2 and in [13], this indicates complex interactions between between CB and electroactive particles. It means that the suspension with lowest or highest LTO amount do not necessarily have the highest or lowest viscosity respectively.

The main focus in determining the contributions to the Li^+ flux from this point will be on the Madec et al. (2014) data. As mentioned, the other two data sets were mainly used to develop an understanding in the SSFB systems and what values are to be expected when studying SSFB suspensions. The Madec

et al. (2014) paper contains both viscosity and electronic conductivity measurements for SSFB suspensions with varying LTO and KB amounts and will therefore be used to further study the behaviour of electroactive material in an SSFB flow cell.

4.2 Resistance for ions and electrons (based on Madec et al. (2014))

From the measured conductivity at different shear rates in a flow cell, the electronic resistance and the ionic potential gradient $\nabla\Phi_2$ can be determined with the help of equations 3.7, 3.8, 3.11 and 3.13. Below, the electronic conductivity data for the LTO-KB suspensions from Madec et al. (2014) can be found at different shear rates in figure 4.5 in the left graph. The Σ in the left graph denotes the measured electronic conductivity in mS cm^{-1}, which will be given the symbol σ in this report.

The electronic conductivity shows complex behaviour under varying shear rates, as can be seen on the left in figure 4.5. At intermediate shear rate, the conductivity shows a minimum for most of the suspensions. As the shear rate is further increases, the conductivity rises again. This behaviour has been reported earlier for carbon black suspensions [19] and as was explained in section 2.1 and is restated here: the electronic conductivity depends on structural evolution of carbon black networks under shear rate. At low shear rates, the viscosity of the suspensions is highest (see for example the left graph of figure 4.4). As explained in section 2.1.4, the carbon additives form long agglomerations at low shear rates, meaning high electronic conductivity. For intermediate shear rates, the long agglomerations are broken into smaller structures, meaning a decrease in electronic conductivity. As the shear rates are further increased, the short agglomerations are constantly loosely connected, allowing for small gaps electrons can tunnel through. This increases the electronic conductivity again. The left graph, extracted from Madec et al. (2014) in figure 4.5 shows that this is indeed the case.

The electronic conductivity profiles that are used to calculate the electronic resistance in the flow cell can be found in Appendix A.2. These profiles are determined by using the calculated velocity profiles in the previous section for each of the Madec et al. (2014) suspensions and calculate the shear rate at each consecutive height y with a part of equation 3.2 ($\dot{\gamma} = \frac{u_x}{dy}$). The height y is broken up in elements dy, the size of which is determined by the amount of datapoints that were extracted per suspension electronic conductivity dataset. This will give shear rate profile. Since the electronic conductivity at each shear rate is known from the left graph in figure 4.5, the electronic conductivity at each shear rate over the height of the flow cell can be plotted, as in appendix A.2.
The right graph in figure 4.5 shows the calculated electronic resistance for each suspension used in the Madec et al. (2014) electrical study. The electronic resistance is shown as a function of the height of the flow cell. From the electronic conductivity profiles shown in Appendix A.2, the electronic resistance can be calculated. This was done by evaluating equation 3.4 and 3.7. The electronic conductivity at each height y in the flow cell can be inserted into equation 3.4. For each electronic resistance layer, as depicted in figure 3.4, the element $dR \cdot A$ can be calculated. In order to calculate the electronic resistance over the height of the flow cell, equation 3.7 must be evaluated by inserting the element $dR \cdot A$. This gives an electronic resistance profile over the height of the flow cell and will allow to determine what the resistance is an electron experiences at a certain height while travelling towards the current collector (placed at $y = 1.4$ mm. The electronic resistance for each of the suspensions used in the electronic conductivity measurements by Madec et al. (2014) is shown in the right graph of figure 4.5. Note that the resistance is given in [$\Omega \cdot m^2$], as the resistance calculation was performed for an element $dR \cdot A$ between two parallel plates. This is the reason $[m^2]$ is also part of the expression, for as was shown in section 3.3, if $A \to \infty$, $R \to 0$, which is meaningless in this system.

Other then the electronic conductivity, the ionic conductivity in 1M LiTFSI propelyne carbonate does not depend on the shear rate. The conductivity of Li^+ in the PC electrolyte has a value of 2×10^{-4} S cm^{-1} [25]. Similar to the determination of the electronic resistance, the external ionic resistance is treated as displayed in figure 3.4. At each height y, the layer in the fluid over the height of the flow cell $R \cdot A$ is assigned to have a conductivity. With equation 3.4, the resistance-surface element $dR \cdot A$ is determined from the conductivity. With equation 3.7 the external ionic resistance of Li^+ in the fluid and near the membrane is calculated. Since the conductivity of Li^+ in the propylene carbonate electrolyte is independent of the shear rate, the ionic conductivity of each layer $dR \cdot A$ in figure 3.4 is the same. This means that when the integral is for the external ionic resistance (equation 3.7) is worked out, the

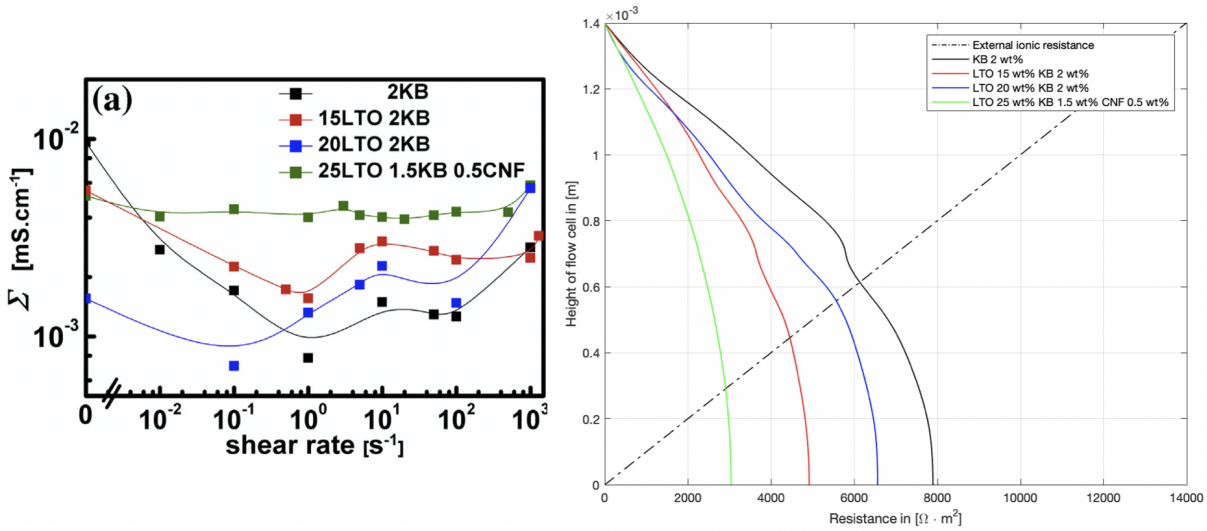

Figure 4.5: The electronic conductivity graph on the left is extracted from Madec et al. (2014). From this graph, the electronic resistance over the height of the flow cell is determined and shown on the right. The resistance is determined as a function of the height in the flow cell. The electronic resistance increases starting from the current collector (at $y = 1.4$ mm) and the external ionic resistance increases from the membrane (at $y = 0$ mm). The potential on the flow cell is $V = 50$ mV.

external ionic resistance will linearly increase. The dashed line in figure 4.5 shows that this is indeed the case. The external ionic resistance however increases starting from the membrane up to the current collector. The reason is that the ions move to the membrane after the redox reaction took place, thus in the exact opposite direction to that of the electrons (which move via the carbon network towards the current collector). The further away a Li^+ is from the membrane, the more resistance it will experience, for it has to travel a larger distance. This too can be seen in figure 4.5.
Figure 4.5 further unveils the suspension containing KB alone gives the highest overall electronic resistance in the flow cell. The electronic resistance decreases as more LTO is added. The LTO-KB suspension containing CNF is nearly shear-rate-independent conductivity and has lowest overall electronic resistance. This can be explained by the microscopic wiring of the smaller aggregates by the flexible CNFs that gives a nearly constant conductivity under shear flow [16].

4.3 Migration (potential gradient)

With the calculated electronical and external ionic resistance and the current I through the flow cell, the contribution to the drop in potential can be calculated with equation 3.5. It should be noted however that the resistance was calculated in $[\Omega \cdot m^2]$, so the current that must be used to determine the potential drop is a current density (in $[A \cdot m^{-2}]$). Equation 3.5 will thus be used in an adjusted form: $V = I" \cdot RA$, where $I"$ denotes the current density.

Three areas are distinguished over which these contributions are determined:

I. Electronic resistance;

II. Internal ionic resistance;

III. External ionic resistance.

Figure 2.5 shows what is meant by these regions. The current density is calculated with equation 2.15 and equation 3.9 to be $I" = 3.68 \times 10^{-8}\ A \cdot m^{-2}$ per electroactive particle. With equation 3.5, the voltage drop over a height y can be calculated. Figure 4.6 shows the result of this calculation.

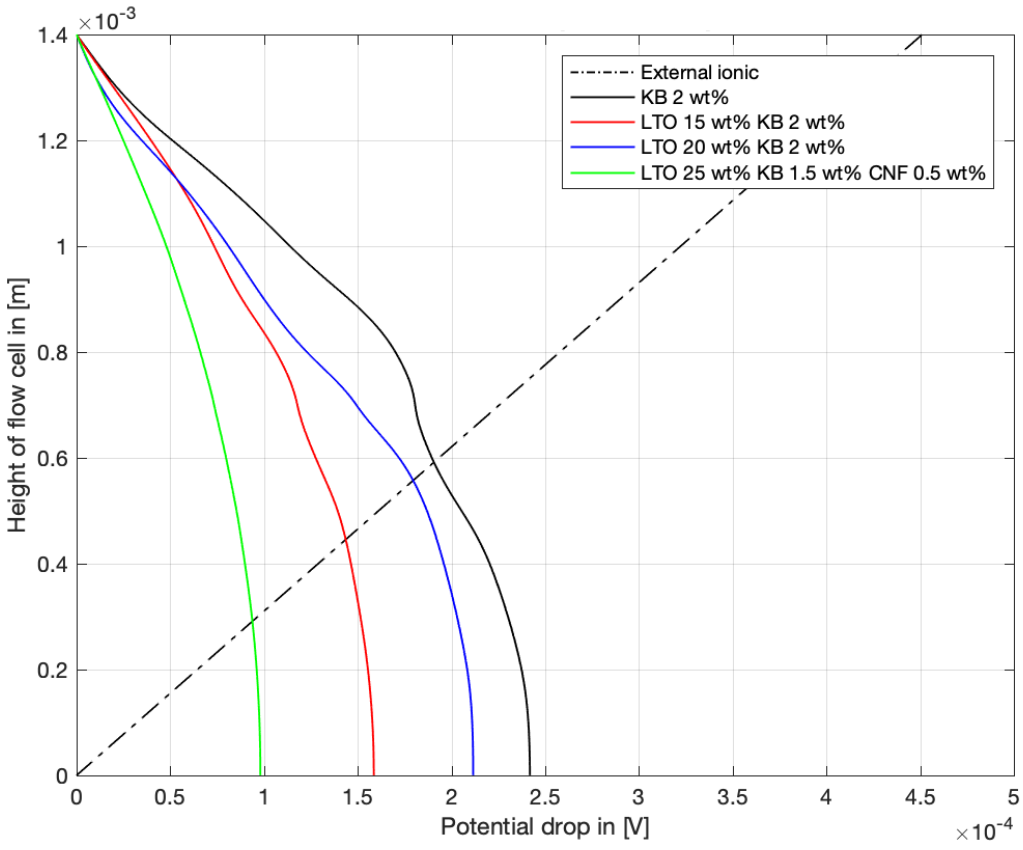

Figure 4.6: Electronic and external ionic potential drop for SSFB suspensions containing KB and LTO in differing amounts. The conductivity data with which this plot is made is extracted from Madec et al. [16]. As indicated in Madec et al. (2014), the applied voltage over the flow cell is V = 100 mV, but because of similarity on both sides of the membrane, the voltage difference over one flow cell is 50 mV. The dashed line represents the ionic potential drop as function of the height of the flow cell. The black, red, blue and green line show the electronic potential drop as a function of the height of the flow cell. As mentioned in section 3.3, it is assumed that the electrons and ions run in a straight line towards the current collector and membrane respectively, and that the flux of both of them is constant.

As indicated in Madec et al. (2014), the applied voltage over the flow cell is V = 100 mV. Due to symmetry on both sides of the membrane, the voltage difference over one flow cell is 50 mV. With this in mind, the contribution of each of the three regions to the potential drop can be determined. The bar graph in figure 4.7 represents these contributions to the total potential drop over one flow cell.

What becomes evident is the significant contribution of the potential drop over the electroactive particle as Li^+ is transported out of the electroactive species. Figure 2.5 shows the expected factors that contribute to the internal resistance Li^+ experiences before being released by LTO. Figure 4.7 is an adjusted version of original image that allows for a better view on the electronic and external ionic contributions to the potential drop. Table 4.1 summarizes what is plotted in figure 4.7.

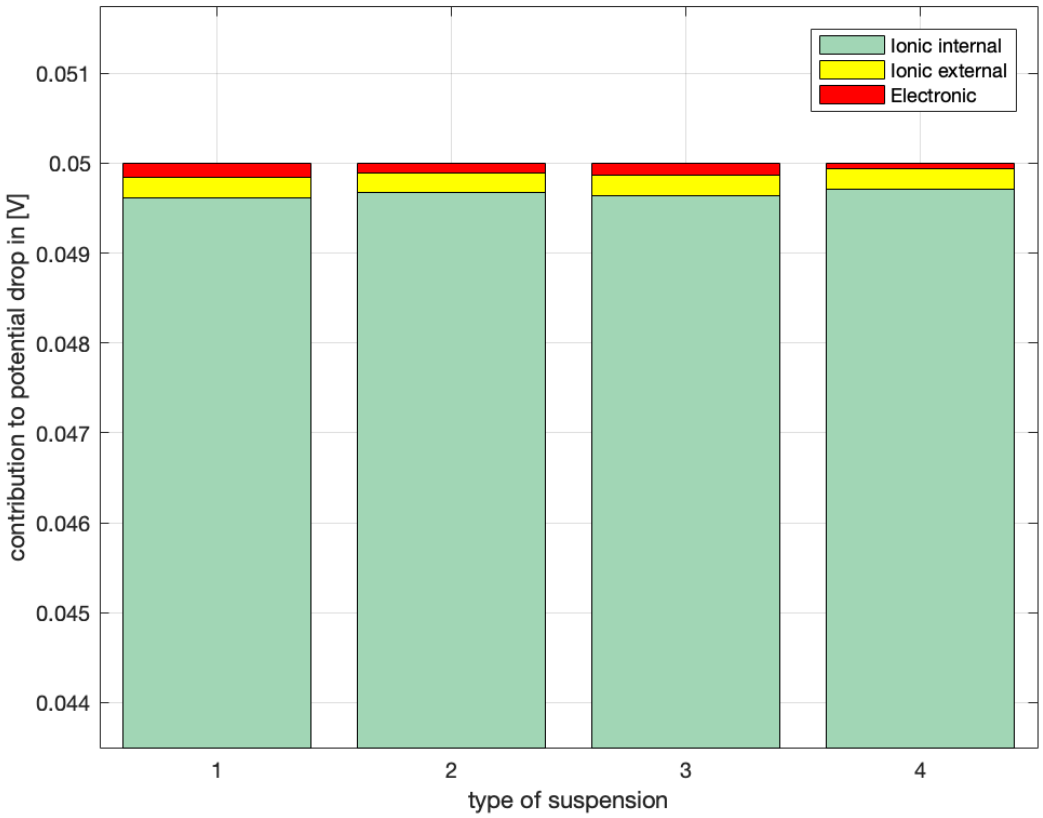

Figure 4.7: Contribution to potential drop for every suspension. Suspension 1 represents the suspension KB 2wt%, suspension 2 LTO 15wt% KB 2wt%, suspension 3 LTO 20 wt% KB 2wt%, suspension 4 LTO 25 wt% KB 1.5wt% CNF 0.5wt%. The internal ionic resistance has the largest contribution to the potential drop in the flow cell, while the external ionic resistance and electronic resistance have minor contributions to the potential drop.

Table 4.1: Table showing data from figure 4.7, visualizing contributions to the potential drop over the flow cell. The top row shows the suspensions, the far-left column lists the contributions to the potential drop. 2KB represents the suspension KB 2wt%, 15LTO2KB represents LTO 15wt% KB 2wt%, 20LTO2KB represents LTO 20 wt% KB 2wt% and 25LTO1.5KB0.5CNF represents LTO 25 wt% KB 1.5wt% CNF 0.5wt%. The potential differences are given in $[mV]$.

	2KB	15LTO2KB	20LTO2KB	25LTO1.5KB0.5CNF
Electronic [mV]	0.157	0.105	0.131	0.0658
External ionic [mV]	0.226	0.226	0.226	0.226
Internal ionic [mV]	49.6	49.7	49.6	49.7

From the electronic and ionic potential drop, the potential gradient in the migration term in the Nernst-Planck equation can be determined. First, the potential drop around the electroactive particle is calculated by using equation 3.11 and inserting the total potential drop over the flow cell to be $V = 50$ mV. With equation 3.13, the potential gradient profile as a function of the height of the flow cell is calculated. The potential gradient at every height y is determined, with y being sectioned into portions Δy. The size of Δy depended on the amount of data points that were extracted from the electronic conductivity plot originating from Madec et al. (2014) (seen in the left graph of figure 4.5). This will give a potential gradient profile over the height of the flow cell.
The potential gradient profile for each of the three different resistances in the flow cell can be determined. From figure 4.6, the electronic potential drop is used to determine $\nabla\Phi_1$, in which 1 represents

the potential gradient for electrons, as explained in section 3.3.
The potential drop due to the internal ionic resistance can be calculated from equation 3.11. The potential drop due to the external ionic resistance is determined by multiplying the external ionic resistance by the calculated current density $I" = 3.68 \times 10^{-8}\ A \cdot m^{-2}$. The current density for ions is the same current density as for electrons, as stated in section 2.3.3, for the flow cell is electrically neutral. The total potential drop $\Delta\Phi_{ionic}$ caused by the resistance an ion experiences can be calculated by adding the both potential drops ($\Delta\Phi_{int,ionic} + \Delta\Phi_{ext,ionic}$). The values can be found by adding up the external ionic and internal ionic potential drops for each of the suspensions in table 4.1.
Now that the ionic potential drop is calculated, equation 3.11 can be used again. This time however, it calculates $\nabla\Phi_2$, in which 2 stands for the ions. It gives the potential gradient profile over the height of the cell and can be used to calculate the migration term in equation 2.8. Since $\nabla\Phi_2$ represents the potential gradient produced by the ions, both the internal and external ionic contributions to the potential drop are taken into account to determine the total $\nabla\Phi_2$. As a function of the height, the ionic potential gradient for each of the four suspensions is plotted in figure 4.8.

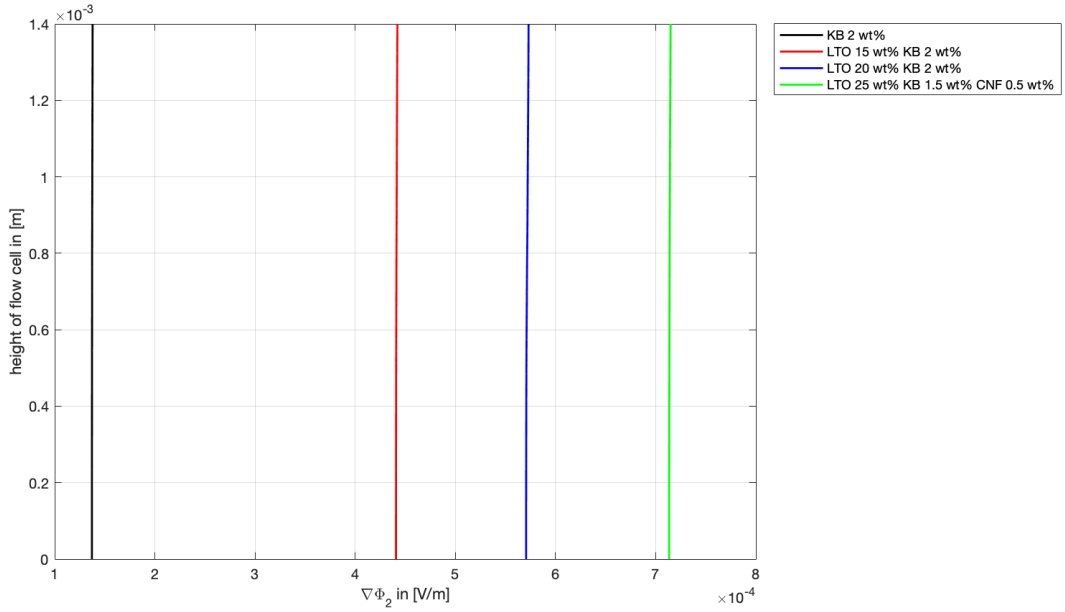

Figure 4.8: Potential gradient for every type of suspension plotted as a function of the height. The potential gradients can be taken to be constant, for there is minimal variation in its values.

The potential gradient is plotted as a function of the height to see if there is any variation of $\nabla\Phi_2$ over the height of the cell. Figure 4.8 shows how the potential gradient profiles $\nabla\Phi_2$ for each of the suspension look like. As can be seen in figure 4.8, the potential gradient profiles seem to be vary minimally. This can be attributed to the potential drop over the electroative species $\Delta\Phi_{ext,ionic}$, which is near constant as can be seen in table 4.1. The potential drop due to external ionic resistance does change, as can be seen in that same table. It is however the substantial contribution of the internal ionic resistance to the overall ionic potential drop that keeps the small variation of the potential gradient due to the external ionic resistance over the height of the flow cell to a minimum. This explains the straight lines in figure 4.8 that represent the ionic potential gradient profiles.

4.4 Total electro-active material flux in a SSFB

The Nernst-Planck equation consists of a migration term, a diffusion term and a convection term. In the above calculation, the contribution due to convection and migration are calculated. As stated in section 2.3.5, the term that contributes to diffusion is taken to be zero, hence the $-D_i \nabla c_i$ term in the Nernst-Planck equation disappears. The Nernst-Planck equation is repeated below to facilitate the following.

$$N_{Li^+} = -z u_{Li^+} F c_{Li^+} \nabla \Phi_2 - D_{Li^+} \nabla c_{Li^+} + c_{Li^+} v \tag{4.1}$$

The valence $z_{Li} = 1$ for the LTO suspension in the redox reaction and the mobility can be found with the relation given in [20]:

$$u_{Li^+} = \frac{D_{Li^+}}{RT}$$

where the diffusion coefficient of Li^+ in propelyne carbonate electrolyte is $D_{Li^+} = 10^{-11}$ m^2 s^{-1} [26]. Inserting the gas constant R and the temperature T = 25°C [16] gives $u_{Li^+} = 4 \times 10^{-11}$ m^2 V^{-1} s^{-1}. F denotes the Faraday constant, which is $F = 96485.3329$ s A mol^{-1}. c_i is the concentration of the Li present, which depends on the weight percentage of LTO in the suspension. The ionic flux due to migration in the y-direction can be calculated with the provided data above.
As was explained in section 3.4.1, the flowing suspension in the flow cell is being pushed forward by the pumps. The total supply of suspension in a slab dx (which can be seen in figure 3.5) is given by the convection in-flux. There will be migration of ions towards the membrane under the influence of the potential set over the flow cell, $V = 50$ mV in this case. The migration flux towards the membrane will be a fraction of the in-flux by convection. To determine how large this fraction will be, the Rohde ratio φ can be calculated with equation 3.15. Before this can be done, the convection and migration terms that can be calculated will be shown. The suspension concentrations must be determined and inserted in the convection and migration terms. Table 4.2 shows what the corresponding concentrations of Li^+-ions are in the suspension (including the Li^+-ions already present in the electrolyte).

Table 4.2: Table showing the concentration of electroactive species in the suspension in [g cm^{-3}].

Suspension	concentration [g cm^{-3}]
KB 2 wt%	0.2871
LTO 15 wt%	0.5294
LTO 20 wt%	0.6337
LTO 25 wt%	0.7466

The convection term for the ionic flux is averaged by determining the convection ionic flux per height y and then taking the average value. The average values for the convection terms are summarized in table 4.3, a table that also includes the migration flux per suspension and the Rohde ratio per suspension, which will be discussed after an explanation about the results shown in figure 4.9.

For the first suspension, the one containing only KB particles and 1 M LiTFSI propylene carbonate electrolyte, the migration term is mostly responsible for the transfer of ions in the flow cell. The velocity profile in figure 4.4 revealed that indeed the maximum velocity of the suspension is significantly smaller than that of the other suspensions. The ion flux of this slow-moving, highly viscous (see figure 4.4) suspension therefore relies mainly on the potential difference in the flow cell. The Li^+ ions that are transported to the membrane are the ions that come from the LiTFSI salt suspended in propylene carbonate. The salt keeps the system electrically neutral. From figure 4.9, it is shown that when there is no electroactive species present, the Li^+-ions from the salt will react to the potential difference set over the flow cell.

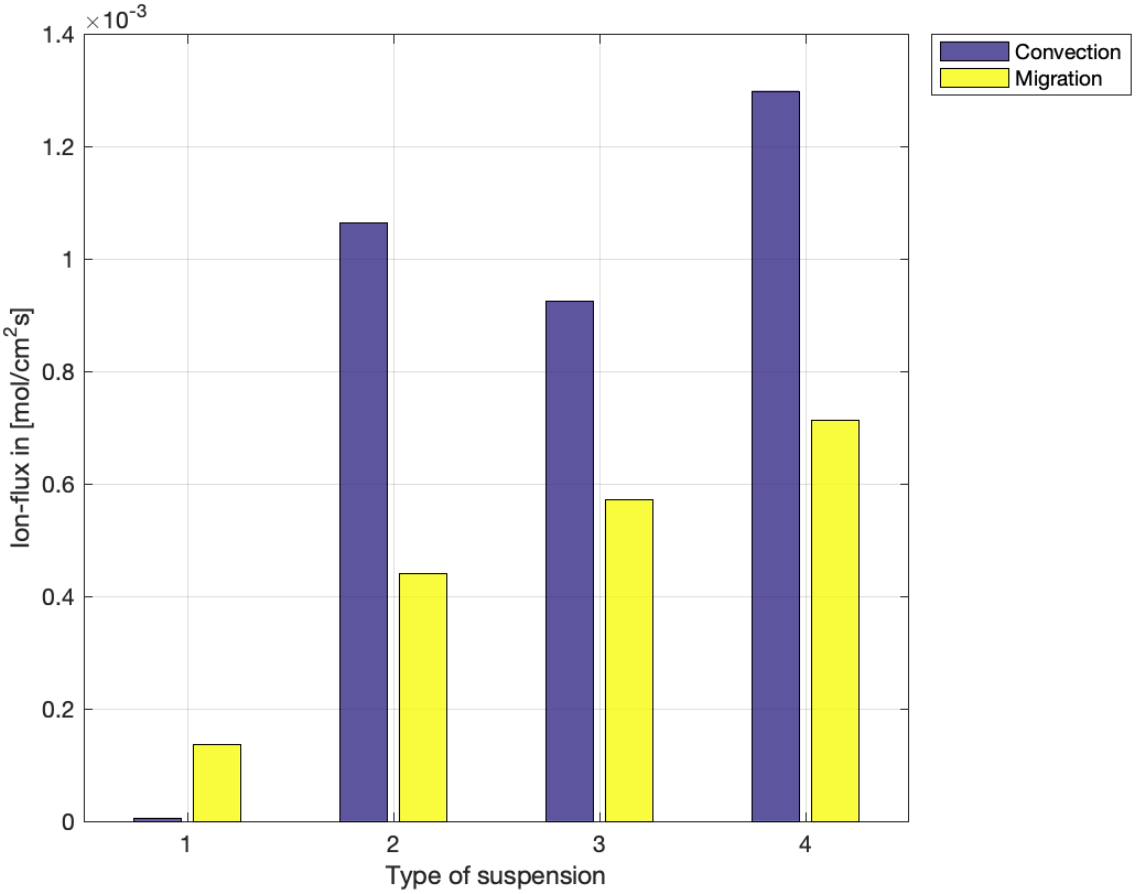

Figure 4.9: Ion flux per suspension in mol cm^{-2} s^{-1}. The migration and convection terms are the only ones considered, the diffusion term has therefore no part in this bar graph. Suspension 1 represents the suspension KB 2wt%, suspension 2 LTO 15wt% KB 2wt%, suspension 3 LTO 20 wt% KB 2wt%, suspension 4 LTO 25 wt% KB 1.5wt% CNF 0.5wt%. The purple bars represent the ionic flux due to convection in the x-direction of the flow cell. The yellow bars show the contribution of migration to the ionic flux. For the suspensions containing $Li_4Ti_5O_{12}$ (LTO) and Ketjen Black particles (suspensions 2, 3 and 4), the yellow bars have a lower maximum than the purple bars, showing that part of the ions flux of convection flows towards the membrane due to migration.

For the three remaining suspensions, the convection term is substantially higher than for the first suspension. As was evident in the velocity profile results in figure 4.4, the enhanced flowability of the LTO-KB suspensions allows for higher velocities of these suspensions. The ionic flux due to convection for LTO-KB suspensions is higher, as can be seen in figure 4.9. The 20LTO2KB suspension, which of the three LTO containing suspensions showed the lowest overall velocity profile as shown in figure 4.4, is the LTO suspension with the lowest convection contribution. As can be seen in figure 4.9, the more electroactive species a suspension contains, the higher the migration towards the membrane is. As the concentration of LTO is increased per suspension, the amount of available Li^+ increases, meaning the contribution to the migration is able to increase per suspension as more LTO is added. Since the potential difference over the flow cell was $V = 50$ mV for all the suspensions it can be concluded that the more available electroactive species present, the higher the contribution to ionic migration towards the membrane.

What remains now is to determine whether the assumption that the electroactive species concentration throughout the flow cell was a valid assumption to make. Section 3.4.1 introduced the Rohde ratio φ, which calculates the fraction of convection that *leaks* away towards the membrane due to migration. It can be calculated with (restated equation 3.15):

$$\varphi = \frac{z_i u_i F \mid \nabla \Phi_2 \mid}{\mid \langle v_x \rangle \mid}. \tag{4.2}$$

The average convection values and the migration values that are used to plot figure 4.9 are shown in table 4.3. The values are shown in [mol cm^{-2} s^{-1}]. The far right column shows the calculated Rhode ratios for the four suspensions.

Table 4.3: Table showing the average convection and, the migration and Rohde ratios of electroactive species in the flow cell per suspension.

Suspension	average convection [mol cm^{-2} s^{-1}]	migration [mol cm^{-2} s^{-1}]	Rohde ratio
KB 2 wt%	$5.9 \cdot 10^{-6}$	$0.14 \cdot 10^{-3}$	23.32
LTO 15 wt%	$1.1 \cdot 10^{-3}$	$0.44 \cdot 10^{-3}$	0.41
LTO 20 wt%	$0.93 \cdot 10^{-3}$	$0.57 \cdot 10^{-3}$	0.62
LTO 25 wt%	$1.3 \cdot 10^{-3}$	$0.71 \cdot 10^{-3}$	0.55

The high Rohde ratio for the first suspension is due to the lack of convection in this suspension. The only Li^+ contributing to any flux are the ions from the LiTFSI salt in propylene carbonate. Thus, despite the convection being very low, there is still migration. This is the reason the Rohde ratio for this suspension is much larger than 1.
For the other three suspensions, the Rohde ratio is of the order 1. This means that a substantial amount of the Li^+-flux in x-direction by convection leaks away towards the membrane due to migration, with the leaking visualized in figure 3.5. As was stated in section 3.4.1, this means that the concentration in the flow cell cannot stay constant, for a significant fraction of convection leaks away due to migration. The assumption that the concentration throughout the flow cell remains constant is herewith proven to be invalid.

5 Discussion

5.1 Semi solid flow batteries

In the development of flow batteries, the efficiency and high energy density of static Li^+-ion batteries should be kept in mind in order to develop battery systems that are a true improvement or enhancement on static and Redox Flow batteries. The energy density of a redox flow battery typically is 40 Wh L^{-1} for a 2M aqueous vanadium RFB, which is low in comparison to conventional static Li^+-ion batteries with energy densities of 100-450 Wh L^{-1}. [4] It means that, since the amount electrochemical energy stored depends on the concentration and volume of the suspension, a great amount of active material and electrolyte is needed to reach the same energy output as static batteries. The semi-solid suspension used by Duduta et al. (2011) has a theoretical energy density of 300-500 Wh L^{-1} which will have a similar energy density range as static batteries after energy losses in the system are accounted for. The SSFB is therefore a valuable improvement of the existing flow battery systems.
The design freedom the RFB systems provided was outbalanced by the use of low-energy density materials, but since SSFB systems are able to deliver similar energy densities as static batteries, the freedom in the design of flow batteries in varying applications is restored. Small systems have mainly been used in determining suspension behaviour in flow cells [4], [13], [16] and [19]. The next steps in the development of SSFB systems are large-scale demonstrations with solid electroactive materials and study how these larger systems can be implemented in applications where large-scale energy storage is needed.

The results gained in this study arose from SSFB simulations with rheological and electrical data of earlier done studies on flow battery suspensions. Instead of doing these measurements with real-life battery systems, rheological and electrical properties of suspensions could be collected via simulations of the suspensions from which the velocity profiles, electronic and ionic resistances and the convection and migration in the flow cell could be determined. It is therefore one of the wishes for the development of (large-scale) SSFB systems to simulate different SSFB suspensions flowing through the system (flow cell, tanks and connecting tubes) [4]. If possible, the simulation provides a helpful hand in understanding SSFB systems and gives rheological and electrical results in less time than measuring directly from a flow cell for which suspensions have to be made. The evaluation of different suspension types with different Carbon Black species could be done in less amount of time and helps reducing costs and increases safety during research. As mentioned, safety for example is one of the issues working with organic solvents as electrolytes, due to their high flammability [4].
Despite simulations being a possibility that could help to push the SSFB system technology forward rapidly, the suspensions themselves form an obstacle. Figures 4.1, 4.2, 4.3, 4.4 and 4.5 show complex rheological and electrical behaviour that is highly dependent on the shear rate and suspension composition. Figure 4.5 reveals that an increase of 5 wt$\%$ of LTO changes the behaviour of the electrical conductivity significantly. Further increasing the amount of LTO but also adding CNF seems to stabilize the conductivity. As mentioned before, this is an indication of complex interactions between Carbon Black and electroactive material. Implementing these suspensions into simulation tends to get difficult, for there is currently an unpredictability in the nature of such suspensions. Thus far, all that has been done is mixing different types of particles to form a suspension that will be tested, which currently comes down to measuring the properties, depending on their composition. Optimizing the amount of active species and carbon black in a certain type of electrolyte would bring the implementation of SSFB systems into electrochemical storage applications closer, but for that to occur, more knowledge must be gained about the interactions between the particles.

5.2 Results

The first point of results discussion is the disregarding of the velocity profile of $\phi_{KB} = 0.034$ in figure 4.1. The maximum velocity of the $\phi_{KB} = 0.034$ suspension was found to be around three times higher in comparison to the velocity profiles of the other three suspensions. Following the trend of the other suspensions, the $\phi_{KB} = 0.034$ suspension should have been the suspension with lowest overall velocity, for it has the highest viscosity per shear rate.
An occurring problem for the determination of the velocity profiles was the over-estimating by the scheme of the values of $\dot{\gamma}_{k+1}$ in equation 3.2. For the scheme, a value of $\dot{\gamma}$ is calculated given a value for the height y and a value for η_{app}. The scheme searches for a value in the provided data set from earlier

research that is closest to this calculated value for $\dot{\gamma}_{k+1}$.
The data of the earlier performed viscosity research on the suspensions (see figures 4.1, 4.2, 4.3 and 4.4) was given on a logarithmic scale. This data is extracted from each of the graphs using a WebPlot-Digitizer [24]. This thus gives viscosity data on a logarithmic scale. The logarithmic distancing between the measurement points is recalculated by taking the inverse logarithm of the extracted data set. Next, interpolation is used to get a viscosity data set with smaller spacing.
Since the original data set was logarithmic, taking a step $\Delta\mu$ in the low $\dot{\gamma}$ regime gives a smaller step in the shear rate than taking a step $\Delta\mu$ in the high $\dot{\gamma}$ regime. So, interpolating the viscosity data at lower $\dot{\gamma}$ gives viscosity points that are less spaced than for higher $\dot{\gamma}$. This also means that in the higher $\dot{\gamma}$ regime, there is more space between the interpolated viscosity data points. So, the calculated $\dot{\gamma}_{k+1}$ has less finer data points to choice from at higher shear rates. This can be solved by further interpolating the data set to provide the scheme with more data points to work with. That way, a finer data set can be used and the iteration scheme of equation 3.2 has more data points to find a value of $\dot{\gamma}$ belonging to an inputted y.

For the choice of Carbon Black particles, Ketjen Black is the preferred option above Super C45 for SSFB suspensions. As discussed in [19], this is because a KB suspension shows a higher flowability and lower electrical percolation thresholds in comparison to C45. Comparing the velocity profiles in figures 4.1 and 4.2 and the conductivity profiles for $\phi_{KB} = 0.021$ and $\phi_{C45} = 0.021$ in Appendix A confirm that KB indeed shows different behaviour compared to C45. Doubling the amount of C45 in a suspension decreases the maximum velocity drastically, indicating a significant elevation in the viscosity. Increasing the conductivity in a suspension by adding more C45 will thus have a negative effect on the pumping energy losses in the system, for a more viscous medium requires more energy to be pushed forward.
To conclude, the better electrically conducting, less viscosity-enhancing KB additive is favored for the use in flow battery suspensions.

The electrical conductivity is highly dependent on the shear rate and in order to optimize it, the intermediate shear rates should be avoided. Intermediate shear rates are responsible for the lowest electrical conductivity values, for the CB network breaks down at these shear rates, reducing the amount of effective chains drastically. One solution to overcome this is using low flow rates which will keep shear rates to a minimum. However, a loss in conductivity at certain regions in the height of the flow cell seems insurmountable, for low shear rates causes the suspensions to become highly viscous (see figures 4.1, 4.2, 4.3 and 4.4). The high dependency of the viscous suspensions on the flow rate require more pumping energy [2] [19], so keeping balance between optimizing conductivity and viscosity must be priority at all times. Losing great amounts of energy to pumping makes the battery overall less efficient, which would pass on the very goal of SSFB systems: developing an *improved* battery system for large-scale energy storage applications.

Figure 4.7 gives insight in the contributions to the electrical and ionic resistance in the system. The internal ionic resistance, consisting of $R_{internal}$, R_{gel} and $R_{boundary}$ as shown in figure 2.5, accounts for the biggest potential drop in the system. This means that the resistance in a SSFB cell is mainly determined by the internal ionic resistance. The transport of Li^+ out of the active species causes the highest resistance in comparison to the electronic and external ionic resistance. Now that the three different resistance regions have been mapped and their values are determined, further research can be done to understand more precisely how they are built up what can be done to improve (reduce) them.

Figure 4.9 reveals what part migration contributes to the transport of ions. As can be seen, the migration increases the more $Li_4Ti_5O_{12}$ a suspension contains. As explained in section 4.4, the presence of more Li^+-ions means more ions react to the potential set over the flow cell, which highers the migration. Figure 4.9 shows that migration causes a significant fraction of the amount of ions from convection in-flux to leak away towards the membrane. This was confirmed by calculating the Rohde ratios for each suspension in table 4.3. The suspension containing only KB had a ratio being much greater than one, which was contributed to the lack of Li^+-ions present, meaning the only ions that could react to the potential over the flow cell were the ions present from the LiTFSI salt dispersed in the propylene carbonate electrolyte.
The other three suspensions had a ratio between $\ll 1$ and 1. As stated in section 3.4.1, the assumption that the Li^+ concentration was valid only for $\varphi \ll 1$. It was assumed that the concentration throughout the flow cell would remain approximately constant, for the concentration of the electroactive species in

the suspensions was high (see table 4.2) and the suspension is constantly being pumped thought the cell. A constant accretion of suspension was assumed to take care of any decreases of the concentration in the flow cell. The results displayed in table 4.3 show otherwise: the assumption that the concentration throughout the flow cell remains constant is invalid. For further research, this must be taken into account, since the concentration appears to be dependent on the axial location in the flow cell.
A final remark on the convection is that for certain concentrations, the flow of the suspensions is enhanced or decreased, meaning that the in-flux of particles is concentration-dependent. It also shows that the power-output of an SSFB is dependent on the flow rate of a suspension, because figure 4.9 shows that the convection for the 15LTO2KB suspension and 25LTO1.5KB0.5CNF suspension have a higher convection contribution to the flux. When comparing this information to what was found in figure 4.4, it becomes clear that the two suspensions with highest overall velocity profile have the highest convection contribution. With this, it can be concluded that ion flux in an SSFB can be tweaked easily by adjusting the pumping force. This way, the power an SSFB can deliver is adjustable (increased or decreased) by pumping the suspension at either higher or lower flow rates, depending on the applications it is used for. Thus, not only does an SSFB form a solution for large-scale energy storage needs, it reveals to be a flexible and adjustable in power delivery should the situation ask so. This confirms what was stated in section 1.3 and section 1.4, that the power of a flow battery is flow rate dependent.

With the results explained in section 4 about the velocity profiles, the electronic and ionic resistances, the potential profiles and the contribution to the ionic flux in the flow cell, more insight is gained in the behaviour of Semi-Solid Flow Battery suspensions. The velocity profiles for suspensions from viscosity—shear rate data used in three different papers were calculated, in order to develop an understanding in the SSFB systems and what values are to be expected when studying SSFB suspensions. Next, the electronic and ionic resistances for LTO-KB suspensions from Madec et al. (2014) were calculated from conductivity-shear rate data. From the resistance, the potential profile was determined, completing what is needed to know to determine what the ionic flux is in the flow cell. Figure 4.9 shows the results and what contributions the convection and migration terms have to the ionic flux. The assumption that the concentration throughout the cell was constant proved to be invalid.

6 Recommendations

In this section, multiple recommendations regarding future research on SSFB systems and semi-solid suspensions are given.

As mentioned in the previous section, simulation of SSFB simulations might be challenging due to the complex rheological and electrical nature of the suspension. It is therefore not recommended to try to simulate the suspensions at this moment, because little is known still about the interactions between the CB particles, the electroactive species and electrolyte containing dissolved salt. This does however set up two ideas for future research which will focus on the microscopic behaviour of the suspensions.

The first recommendation is to look into the interactions between the CB particles and active species to determine and predict how the combination of them will behave. As indicated multiple times throughout this report, there is a complex interaction of the CB particles with the active species. LCO in combination with KB gives a relatively high viscosity, as can be seen in figure 4.3, while the suspension containing KB only has significantly lower viscosity. A look at figure 4.4 however shows that a LTO-KB combination is less viscous than a suspension containing KB alone. It should be noted that the fraction of KB in the suspensions used for the measurements and calculations shown in figure 4.3 is substantially lower than the fraction of KB in the suspensions used for the measurements and calculations shown in figure 4.4. Keeping in mind there needs to be a balance between both the rheological and electrical properties of a semi-solid suspension, the interactions between the active species and CB particles can be further investigated. This can for example be done by fabricating multiple semi-solid suspensions with differing types and amount of electroactive material and varying amount of KB particles. Rheological and electrical studies that are used for this report can be performed. Together with a Scanning Electron Microscope, the formation of the suspensions can be studied and linked more profoundly to the flow and conductivity profiles.

Closely related to this interaction is the second recommendations, which focuses on the resistances in the flow cell. Figure 2.5 schematically showed where the different types of contributions to the overall resistance for electrons and ions in a SSFB cell come from. In this thesis, the resistances were separated into three areas for which resistances studies were performed. The three areas were; $R_{electronic}$, which represents the resistance the electrons experience as they are transported via the Carbon Black network; $R_{int,ionic}$ which represents the resistance an ion experiences as it is transported out of the electroactive particle; $R_{ext,ionic}$, which represents the resistance an ion experiences as it moves through the electrolyte fluid towards the membrane of the flow cell. The resistance three regions can be further divided into separate resistances that contribute to $R_{electronic}$, $R_{int,ionic}$ or $R_{ext,ionic}$. Now that is calculated for LTO-KB suspensions what the values for each of these three resistances in the flow cell are, it is recommended to study in more detail how each of these three resistances are built up and how they are influenced by the flow of the suspensions.

The last recommendation that will be given is the testing of SSFB on large-scale, an idea that was also proposed by Qi et al. (2017) in [4]. Microscopic behaviour of flowing media often differs from macroscopic behaviour, which is why it is useful to make large-scale demonstrations of SSFB systems to see how they will perform and hold in more realistic situations. More realistic estimates of operating parameters can be determined. Adviced is to make an SSFB model of intermediate size and study how it operates and how the semi-solid suspension behaves.

7 Conclusions

The goal of this study was to investigate flux behaviour of active species and their resistance to movement in a Semi-Solid Flow Battery Cell and determine how it is influenced by different suspension concentrations, varying flow rates and various amounts and types of electroactive material. This was done by evaluating different components of the Nernst-Planck equation with viscosity and conductivity data at different shear rates from earlier done research on flowing semi-solid suspensions.

The resistance in the system is found to be determined mainly by the internal ionic resistance. It is recommended to study more closely how this resistance is built-up and what can be done to optimize it in favor of battery efficiency. This can be done by studying the microscopic interactions between the electrolyte with dissolved salt, Carbon Black particles and electroactive material, which will also help in developing an improved understanding of the rheological and electrical behaviour of the suspensions.

Calculations have shown that the contributions of migration and convection massa transport in a slab of $dx \cdot L$ depend strongly on the concentration and flowability of Carbon Black particles and electroactive material in Semi-Solid Flow Batteries. The flowability of the suspensions depend on complex interactions of electroactive species with the Carbon Black particles. The more electroactive species a suspension contains, the higher the contribution to the migration of ions towards the membrane. It was found that the assumption that the Li^+ concentration of the suspensions throughout the cell remains constant was invalid, for a significant fraction of the convection in-flux leaked away to the ionic membrane due to migration.
The ionic flux due to convection is adjustable, as it depends on the flow rate of the suspension. With this, the power an SSFB can deliver is adjustable, which shows that SSFB systems form a valuable and flexible solution for large-scale energy storage needs.

Bibliography

[1] Brunini, V., Chiang, Y.M., Carter, W.. (2013). Modeling the hydrodynamic and electrochemical efficiency of semi solid flow batteries. *Electrochimica Acta. 69, pp. 301-307*. 10.1016/j.electacta.2012.03.006.

[2] Weber, A.Z., Mench, M.M., Meyers, J.P. et al. (2011). Redox flow batteries: a review. *J Appl Electrochem 41, 1137*. https://doi.org/10.1007/s10800-011-0348-2

[3] Gao, L., Liu, S. (2002). Dynamic Lithium-Ion Battery Model for System Simulation. *IEEE Transactions on Components and Packaging Technologies, vol. 25, No. 3, sept 2002.*

[4] Qi, Z., Koening, G.M. (2017). Review Article: Flow battery systems with solid electroactive materials. *Journal of Vacuum Science and Technology B 35, 040801* https://doi.org/10.1116/1.4983210

[5] B. Kennedy, D. Patterson, S. Camilleri. (2000). Use of lithium-ion batteries in electric vehicles. *Journal of Power Sources, Volume 90, Issue 2, 2000, Pages 156-162.* https://doi.org/10.1016/S0378 7753(00)00402 X

[6] S. Megahed, W. Ebner. (1995). Lithium-ion battery for electronic applications. *Journal of Power Sources, Volume 54, Issue 1, 1995, Pages 155-162* doi.org/10.1016/0378 7753(94)02059 C.

[7] Cruve, G., Mardikian, P., Marcoux, L., (1997). 50 to 100 Ah lithium-ion cells for aircraft and spacecraft applications. *Journal of Power Sources, vol. 65, pp. 149-153.*

[8] Majima, M., Ujiie, S., Yagasaki, R., Koyama, K., Inazawa, S. (2001). Development of long life lithium ion battery for power storage. *Journal of Power Sources, vol. 101, pp. 53-59, 2001.*

[9] Klein, R., Chaturvedi, N. A., Christensen, J., Ahmed, J., Findeisen, R. and Kojic, A. (2013). *Electrochemical Model Based Observer Design for a Lithium-Ion Battery. IEEE Transactions on Control Systems Technology, vol. 21, no. 2, pp. 289-301, March 2013*. doi: 10.1109/TCST.2011.2178604.

[10] Megahed, S., Scrosati, B., (1994). Lithium-ion rechargeable batteries. *Journal of Power Sources, Volume 51, Issues 1 2, 1994, pp. 79-104.* https://doi.org/10.1016/0378 7753(94)01956 8.

[11] Kown, N.H., Mouck-Makanda, D., Fromm, K.M. (2018). A Review: Carbon Additives in LiMnPO4- and LiCoO2-Based Cathode Composites for Lithium Ion Batteries. *Batteries, vol. 4, No. 4*. https://www.mdpi.com/2313 0105/4/4/50

[12] Van den Akker, H., Mudde, R.F., (2014). *Transport Phenomena: The Art of Balancing*. Delft, the Netherlands. Published by Delft Academic Press/VSSD.

[13] Duduta, M., Ho, B., Wood, V.C., Limthongkul, P., Brunini, V.E., Carter, W.C., Chiang, Y.M., (2011). Semi-Solid Lithium Rechargeable Flow Battery. *Adv. Energy Mater. 2011, XX, pp. 1–6* https://doi.org/10.1002/aenm.201100152

[14] Chiang, Y.M., Craig Carter, W., Ho, B.H., Duduta, M. (2010). High density redox flow device. *WO Patent WO/2009/151639*

[15] Biendicho, J.J., Flow, C., Sanz, L., Morante, J.R. (2016). Static and Dynamic Studies on $LiNi_{1/3}Co_{1/3}Mn_{1/3}O_2$-Based Suspensions for Semi-Solid Flow Batteries. *ChemSusChem, vol. 9, pp. 1938-1944, 2016.*

[16] Youssry, M., Madec, L., Soudan, P., Cerbelaud, M., Guyomard, D., Lestriez, B., (2014). Formulation of flowable anolyte for redox flow batteries for redox flow batteries: Rheo-electrical study. *Journal of Power Sources, vol. 274, pp. 424-432, 2015.*

[17] Solomon, B.R., Chen, X., Rapoport, L., Helal, A., McKinley, G.H., Chiang, Y.M., Varansi, K., (2018). Enhancing the Performance of Viscous Electrode-Based Flow Batteries Using Lubricant-Impregnated Surfaces. *ACS Appli. Energy Matter. No. 1, pp. 3614-3621, 2018.*

[18] Madec, L., Youssry, M., Cerbelaud, M., Soudan, P., Guyomard, D. and Lestriez, B. (2015), Surfactant for Enhanced Rheological, Electrical, and Electrochemical Performance of Suspensions for Semisolid Redox Flow Batteries and Supercapacitors. *ChemPlusChem, 80: 396-401*. doi:10.1002/cplu.201402042

[19] Youssry, M., Madec, L., Soudan, P., Cerbelaud, M., Guyomard, D., Lestriez, B., (2013). Non-aqueous carbon black suspensions for lithium-based redox flow batteries: rheology and simultaneous rheo-electrical behavior. *Phys Chem Chem Phys. 2013;15(34):14476-14486*. doi:10.1039/c3cp51371h

[20] Knehr, K.W., Agar, E., Dennison, C.R., Kalidindi, A.R. and Kumbur, E.C., (2012). A Transient Vanadium Flow Battery Model Incorporating Vanadium Crossover and Water Transport through the Membrane. *Journal of The Electrochemical Society, vol. 159, No. 9, A1446-A1459*.

[21] Eriksson, T. (2001). LiMn2O4 as a Li-Ion Battery Cathode. From Bulk to Electrolyte Interface. *Acta Universitatis Upsaliensis. Comprehensive Summaries of Uppsala Dissertations from the Faculty of Science and Technology 651. 53 pp. Uppsala.*

[22] Liu, A.L. Shafiei, M., Ledwich, G., Miller, W. and Nourbakhsh, G. (2017) Correlation study of residential community demand with high PV penetration. *Australasian Universities Power Engineering Conference (AUPEC), Melbourne, VIC, 2017, pp. 1-6.*

[23] Dennsion, C.R., Beidaghi, M., Hatzell, K.B., Campos, J.W., Gogotsi, Y., Kumbur, E.C., (2014). Effects of flow cell design on charge percolation and storage in the carbon slurry electrodes of electrochemical flow capacitors. *Journal of Power Sources 247, feb 2014, pp. 489-496*. https://doi.org/10.1016/j.jpowsour.2013.08.101

[24] Rohatgi, A., (2019). WebPlotDigitizer. Version 4.2. *https://automeris.io/WebPlotDigitizer*, San Fransisco, California, USA.

[25] Jayathilake, P.A.R.D., Dissanayake, M.A.K.L., Albinsson, I., Mellander, B.-E., (2003). Dielectric relaxation, ionic conductivity and thermal studies of the gel polymer electrolyte system PAN/EC/PC/LiTFSI. *Solid State Ionics Volume 156, Issues 1–2, January 2003, Pages 179-195*.

[26] Jung, H.-G., Venugopal, N., Scrosati, B., Sun, Y.-K. (2013). A high energy and power density hybrid supercapacitor based on an advanced carbon-coated Li4Ti5O12 electrode. *Journal of Power Sources, vol. 221, pp. 266-271.*

[27] MATLAB. (2016). version 9.0.0 (R2016a). Natick, Massachusetts: The MathWorks Inc.

A Conductivity profiles

A.1 Conductivity profile KB and C45

Below, the two conductivity profiles can be found as referred to in section **??**. The conductivity profiles are given for KB and C45 with equal volume fractions ϕ. What becomes clear is the significantly higher overall conductivity of KB in a flow cell compared to C45, despite volume fractions being equal. This confirms the earlier discussed the lower electrical percolation threshold for KB over C45 [19].

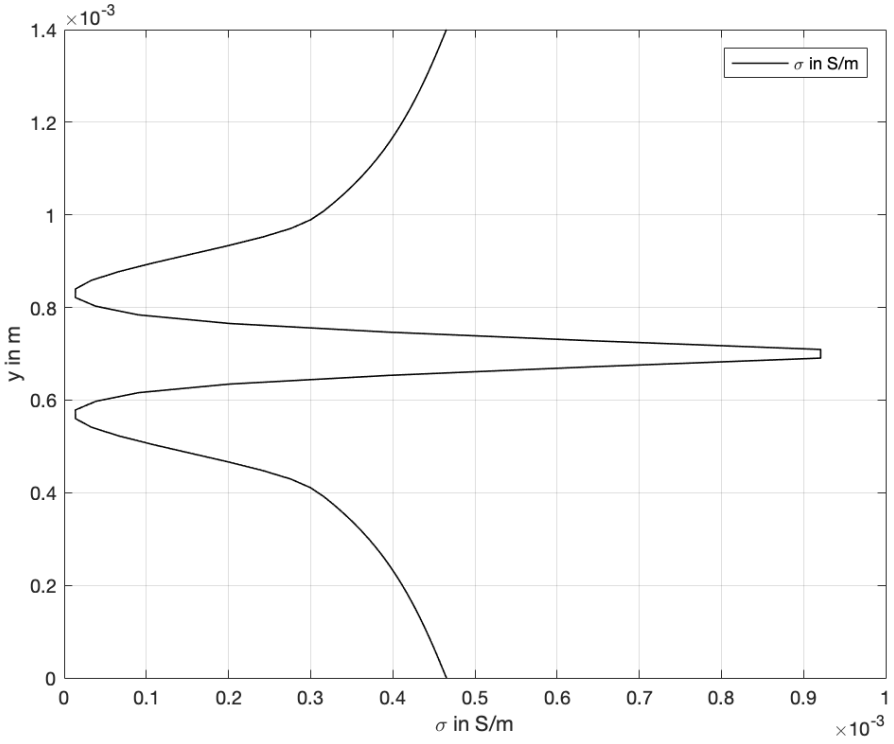

Figure A.1: Conductivity in the flow cell for suspension $\phi_{KB} = 0.021$.

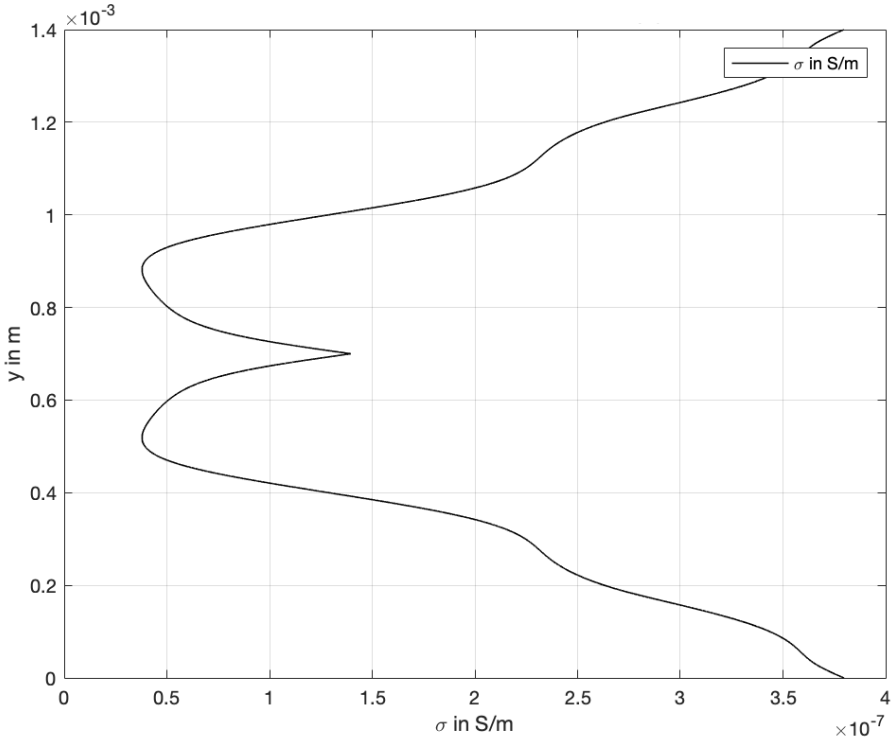

Figure A.2: Conductivity in the flow cell for suspension $\phi_{C45} = 0.021$.

A.2 Conductivity profiles Madec data

The conductivity profiles found in this appendix are determined with the data shown in figure 4.5. In each of the following four plots, the conductivity of Li^+ is plotted as well to ease the comparison of its value to the electronic conductivity. The conductivity of Li^+ in a propelyne carbonate electrolyte is 2×10^{-4} S cm^{-1}.
As can be seen in [19], the conductivity of the suspensions is highly dependent on the shear rate. As mentioned in this paper, there are shear rate regions where CB agglomerates form such networks that the conductivity rises, while other shear rate regions do not allow for these networks to form (or less optimally). This explains the decrease of the conductivity in intermediate regions of shear rate.

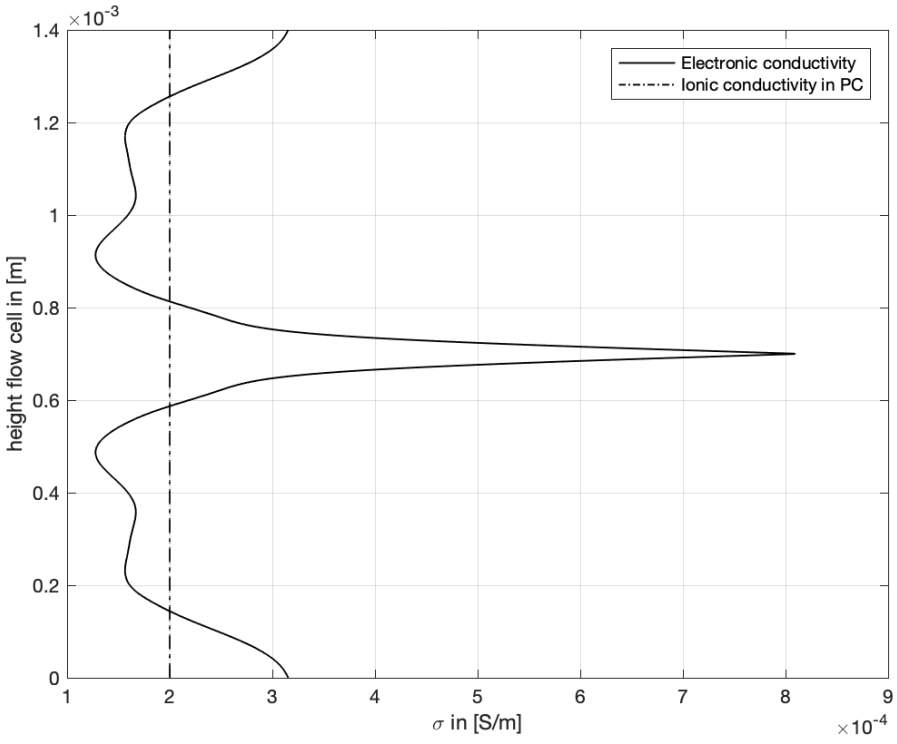

Figure A.3: Conductivity in the flow cell for suspension KB 2 wt%.

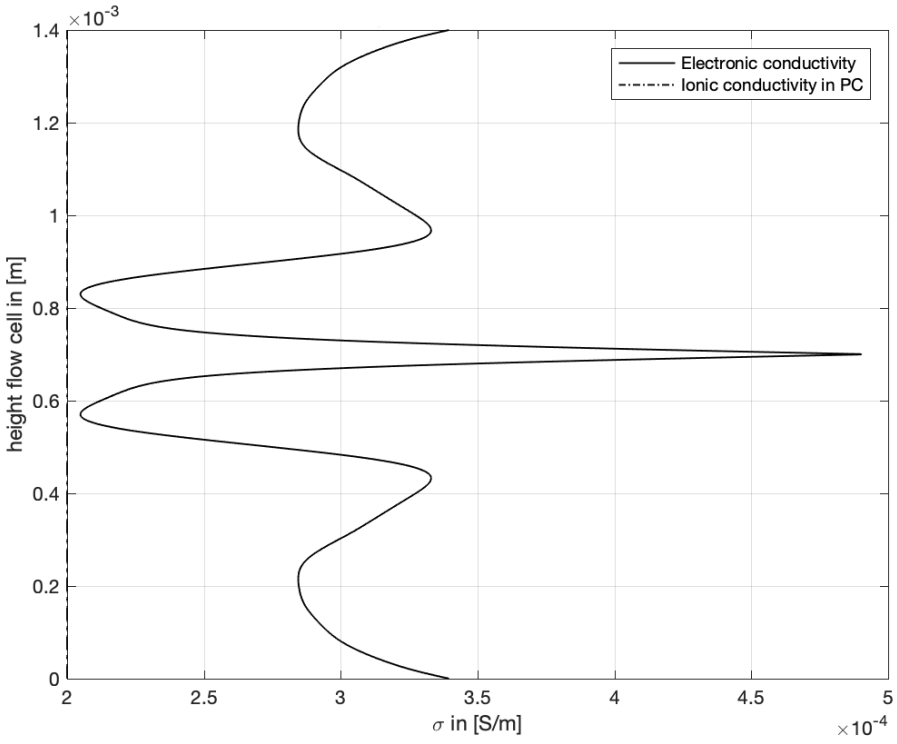

Figure A.4: Conductivity in the flow cell for suspension LTO 15 wt% KB 2 wt%. The conductivity of Li^+ is nearly on the y-axis, showing this suspension has higher overall conductivity.

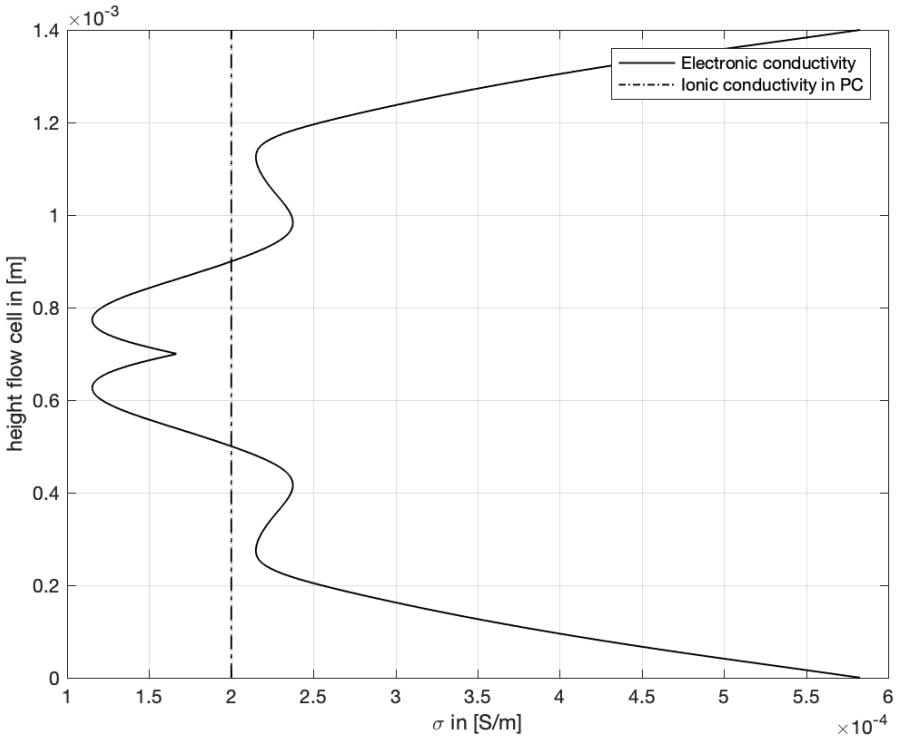

Figure A.5: Conductivity in the flow cell for suspension LTO 20wt% KB 2 wt%.

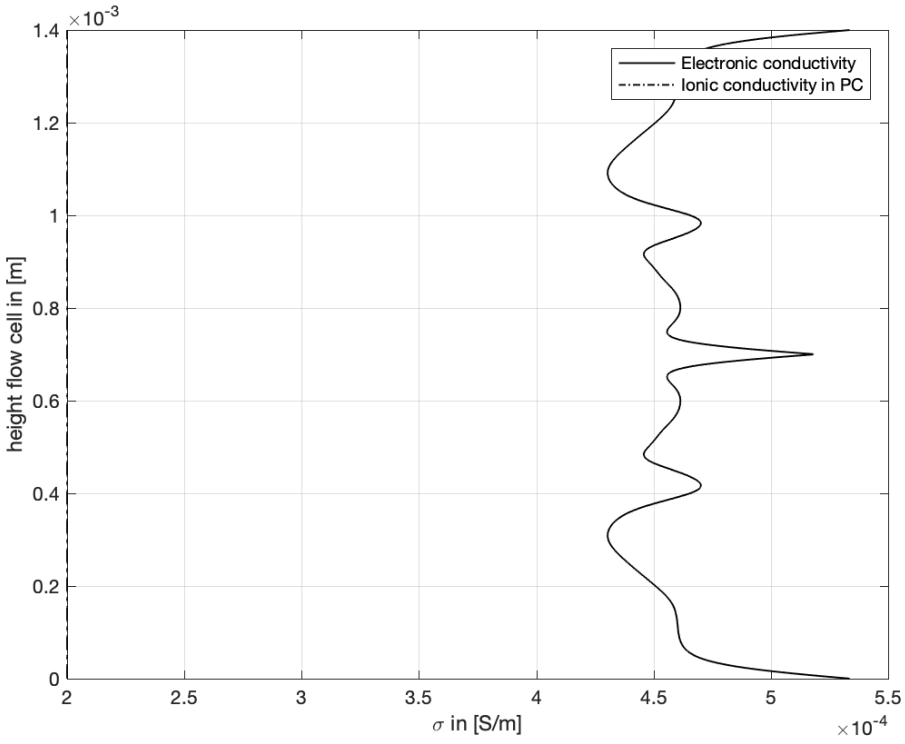

Figure A.6: Conductivity in the flow cell for LTO 25 wt% KB 1.5 wt% CNF 0.5 wt%. The conductivity of Li^+ is nearly on the y-axis, showing this suspension has higher overall conductivity.

B Simulation near membrane

In the Knehr et al. (2012) paper, a special region for the ion flux is treated. A model is developed that discusses and determines the ion flux in the region where the electrolyte and membrane intersect. It is thought and assumed in this paper that the contributions to the Nernst-Planck equation are dominated by the migration and diffusion term, the last of which was disregarded in this report. In this appendix, the model and its results for the Madec et al. (2014) data used in this report are discussed briefly and given as a recommendation in the development of simulating flux behaviour of electroactive material in an SSFB.
The model starts with making a distinction in different region for ion flux. The electrolyte—membrane interface is of interested, with a certain thickness δ over which the model should hold as can be seen in figure B.1. This region is treated separately, because as is stated in [20], the dissolving of the active species in the membrane produces a discontinuity over the interface in ion concentration. The model tries to overcome the discontinuity.

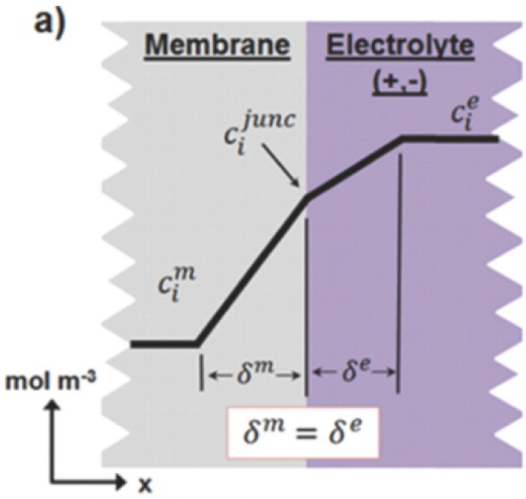

Figure B.1: Visual representation of a region of finite thickness in the electrolyte—membrane interface. [20] c_i^m denotes the concentration of active species in the membrane, c_i^{junc} the concentration of the active species at the electrolyte—membrane junction, c_i^e the concentration of active species in the electrolyte and $\delta^{e,m}$ denotes the regime in which the model holds.

Because the steep concentration and migration gradients cause at the interface cause large diffusion and migration fluxes, the contribution of convection to the total species flux is negligible. Furthermore, since δ is typically less than 1% of the membrane thickness, linear variations in concentration and potential over these small regions are assumed. With these two assumptions, the diffusion and migration terms of Nernst-Planck equation can be discretized as follows:

$$N_i^{er} = -D_i^{eff}\frac{(c_i^e - c_i^{junc})}{\delta^e} - z_i u_i^e F \frac{(c_i^e + c_i^{junc})}{2}\frac{K_\phi(\phi_l^e - \phi_l^m)}{\delta^e} \tag{B.1}$$

$$N_i^{er} = -D_i^m\frac{(c_i^{junc} - c_i^m)}{\delta^m} - z_i u_i^m F \frac{(c_i^{junc} + c_i^m)}{2}(1 - K_\phi)\frac{(\phi_l^e - \phi_l^m)}{\delta^m} \tag{B.2}$$

where N_i^{er} and N_i^{mr} are the fluxes of species i in the electrolyte interface region and membrane interface region, respectively. The concentration of species i at the electrolyte—membrane interface is represented by c_i^{junc}, D_i^m is the diffusivity of the active species in the membrane, K_ϕ is a fitting parameter that represents the percentage of the total potential drop $(\phi_l^e - \phi_l^m)$ occurring in the electrolyte interface region. ϕ_l denotes the liquid potential in the flow cell. The potential drop is found by using the Donnan potential:

$$\Delta\phi = \phi_l^e - \phi_l^m = \frac{RT}{F} ln(\frac{c_i^e}{c_i^m}) \tag{B.3}$$

The ionic mobility in the electrolyte u_i^e is represented by the Nernst-Einstein equation, which is as follows:

$$u_i^e = \frac{D_i^{eff}}{RT}. \tag{B.4}$$

The D_i^{eff} stands for the effective diffusive constant of the active species in electrolyte. The electrolyte flows through the flow cell that has a certain porosity ϵ, which stands for the ease with which a particle can diffuse trough its surrounding medium. D_i^{eff} is calculated with:

$$D_i^{eff} = \epsilon^{3/2} \cdot D_i \tag{B.5}$$

in which D_i is the diffusive coefficient of the active species in the electrolyte.
The concentration of active species at the electrolyte—membrane interface c_i^{junc} can be found be setting the fluxes at the interface equal $N_i^{er} = N_i^{mr}$. Next is to insert all parameters to determine what the ion fluxes are for the suspensions in the region. The following will be a summary of all the values that are used. The porosity ϵ=0.093 and $D_i^m = 5 \times 10^{-12}$ m^2 s^{-1} and c_i^m = 1000 mol m^{-3} for a Nafion Membrane [22], $D_i^e = 10^{-1}$ m^2 s^{-1} [26], T = 298 K [16], R = 8.314 J mol^{-1}, z_i = 1 and $\delta_e = \delta_m = 1$ μm [20].
The result can be found in figure B.2.

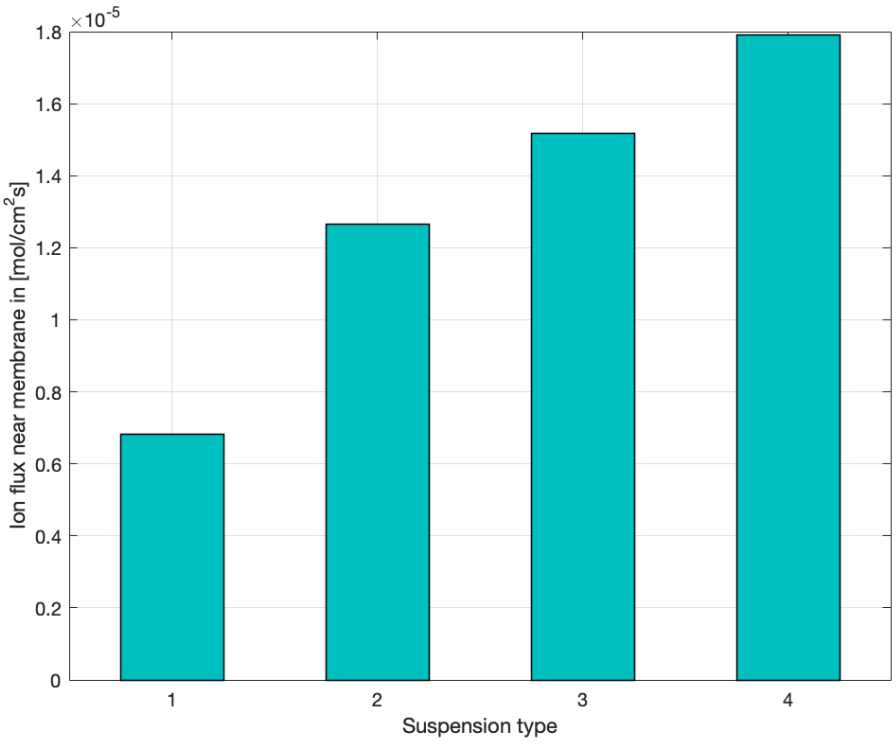

Figure B.2: Ion flux in the electrolyte—membrane interface. Suspension 1 represents the suspension KB 2wt%, suspension 2 LTO 15wt% KB 2wt%, suspension 3 LTO 20 wt% KB 2wt%, suspension 4 LTO 25 wt% KB 1.5wt% CNF 0.5wt%.

When these results are compared to the results shown in figure 4.9, what stands out is the significant difference between the values of the ion fluxes. As mentioned by Knehr et al. (2012), this could be due to the disregarding of the convection term in this model. As can be seen in figure 4.9, the convection term contributes substantially to the ion flux in the flow cell. Another factor could be that the potential that was set over the flow cell in Madec et al. (2014) is greater than the potential drop determined via Knehr et al. (2014). Knehr et al. tried to simulate a migration stimulated by a concentration difference of active species in the electrolyte and the membrane. Madec et al. (2014) imposed another potential over the flow cell, which was a stronger potential than could be calculated by Knehr et al. (2014). This is in line with comparing figure 4.9 with figure B.2, for the contribution of the migration term alone for

the Madec et al. (2014) LTO-KB suspensions alone is greater than the total ion flux from migration and diffusion for Knehr et al. (2014).

C SSFB images

Figure C.1: An example of the suspensions used in Duduta et al. (2011). The fluid semi-solid suspension contains $LiCoO_2$ powder as the active material and Ketjen black as the conductive material, dispersed in alkyl carbonate electrolyte. The respective volumes and concentrations are unknown. [13]

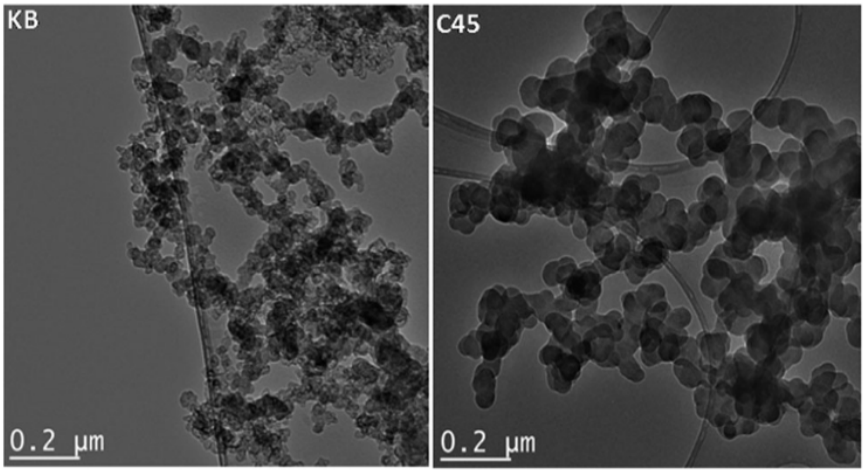

Figure C.2: TEM micrographs of Ketjen Black (left) and Super C45 (right). [19]

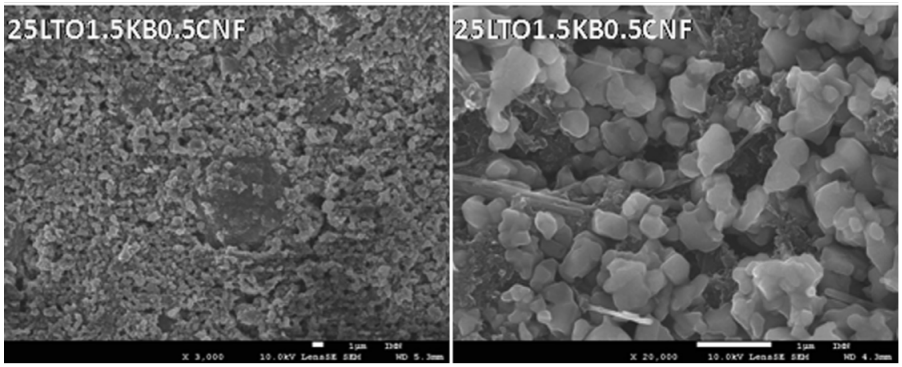

Figure C.3: SEM micrographs of LTO2KB suspensions and carbon nanofibers-containing suspension. In these micrographs, LTO is white and KB is black. [16]

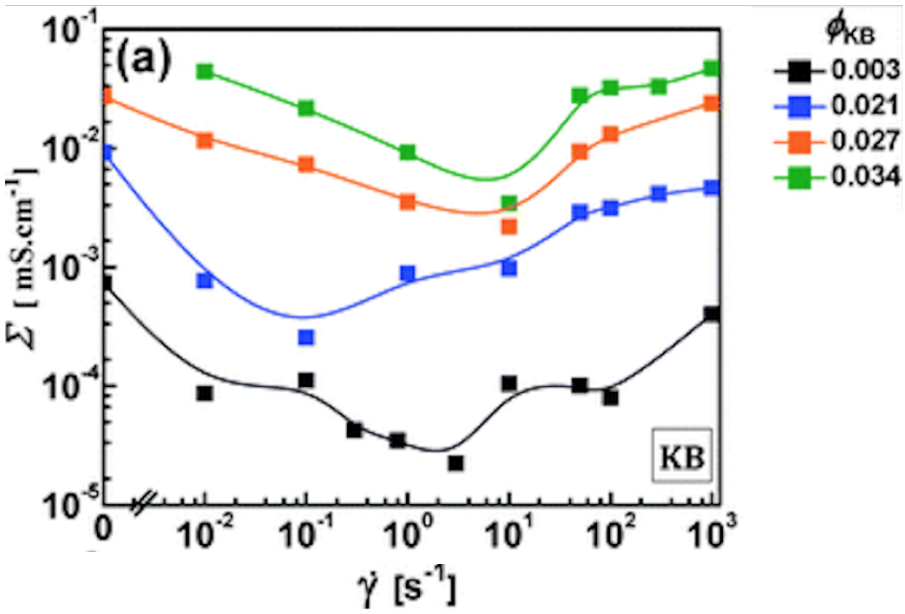

Figure C.4: Adjusted version of Fig. 8 in [19] showing the conductivity Σ measurements at different shear rates for suspensions containing different volume fractions of KB. The electrolyte is 1 M LiTFSI in propylene carbonate at 25°C.